BIOCHEMISTRY
including biophysical chemistry & molecular biology

Article

pubs.acs.org/biochemistry

Plasticity in the High Affinity Menaquinone Binding Site of the Cytochrome aa_3-600 Menaquinol Oxidase from *Bacillus subtilis*

Sophia M. Yi,[§] Alexander T. Taguchi,[†,‡,▽] Rimma I. Samoilova,[⊥] Patrick J. O'Malley,[*,∥] Robert B. Gennis,[*,§,†] and Sergei A. Dikanov[*,‡]

[§]Department of Biochemistry, University of Illinois at Urbana−Champaign, Urbana, Illinois 61801, United States

[†]Center for Biophysics and Computational Biology, University of Illinois at Urbana−Champaign, Urbana, Illinois 61801, United States

[⊥]V. V. Voevodsky Institute of Chemical Kinetics and Combustion, Russian Academy of Sciences, Novosibirsk 630090, Russian Federation

[∥]School of Chemistry, The University of Manchester, Manchester M13 9PL, U.K.

[‡]Department of Veterinary Clinical Medicine, University of Illinois at Urbana−Champaign, Urbana, Illinois 61801, United States

Supporting Information

ABSTRACT: Cytochrome aa_3-600 is a terminal oxidase in the electron transport pathway that contributes to the electrochemical membrane potential by actively pumping protons. A notable feature of this enzyme complex is that it uses menaquinol as its electron donor instead of cytochrome *c* when it reduces dioxygen to water. The enzyme stabilizes a menasemiquinone radical (SQ) at a high affinity site that is important for catalysis. One of the residues that interacts with the semiquinone is Arg70. We have made the R70H mutant and have characterized the menasemiquinone radical by advanced X- and Q-band EPR. The bound SQ of the R70H mutant exhibits a strong isotropic hyperfine coupling ($a^{14}_N \approx 2.0$ MHz) with a hydrogen bonded nitrogen. This nitrogen originates from a histidine side chain, based on its quadrupole coupling constant, e^2qQ/h = 1.44 MHz, typical for protonated imidazole nitrogens. In the wild-type cyt aa_3-600, the SQ is instead hydrogen bonded with N_ε from the Arg70 side chain. Analysis of the ^{1}H 2D electron spin echo envelope modulation (ESEEM) spectra shows that the mutation also changes the number and strength of the hydrogen bonds between the SQ and the surrounding protein. Despite the alterations in the immediate environment of the SQ, the R70H mutant remains catalytically active. These findings are in contrast to the equivalent mutation in the close homologue, cytochrome bo_3 ubiquinol oxidase from *Escherichia coli*, where the R71H mutation eliminates function.

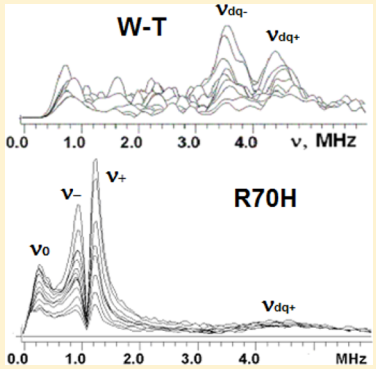

Bacillus subtilis cytochrome aa_3-600 menaquinol oxidase is one of several terminal oxygen reductases present in the respiratory chain in the *B. subtilis* membrane. During its catalytic cycle, cyt aa_3-600 reduces dioxygen to water while actively pumping protons across the membrane. The overall result is to generate an electrochemical membrane potential that is utilized for ATP synthesis. This enzyme is the predominant oxygen reductase present in *B. subtilis* during aerobic growth.[1−4] Cyt aa_3-600 is a member of the A-family of heme−copper respiratory oxygen reductases, which includes bovine mitochondrial cytochrome *c* oxidase and *Escherichia coli* cyt bo_3 ubiquinol oxidase. One motivation of the current work is to compare the specific protein interactions that favor the catalytic oxidation of menaquinol in cyt aa_3-600 vs the oxidation of ubiquinol by cyt bo_3. Despite differences in electron donating species (quinone vs cytochrome *c*) and different types of redox centers (Cu_A, heme *a*, heme *b*, heme *o*), oxygen reductases belonging to the heme−copper superfamily share a common mechanism for reducing dioxygen to water and for pumping protons.

Cyt aa_3-600 does not interact with cyt *c* and lacks the Cu_A redox site in subunit II that is a common feature in cyt *c* oxidases.[2,5] Instead, cyt aa_3-600 accepts electrons from menaquinol initially at a low-spin heme *a*, which then passes them to the catalytic site composed of high-spin heme a_3 and Cu_B, where O_2 is reduced to water. Menaquinone (MQ), predominantly with seven isoprene units in its side chain, is present in the membrane of *B. subtilis*, which does not contain ubiquinone (UQ).[6] Both MQ and UQ can act as either a one-electron or two-electron redox partner and have three redox states: fully oxidized, one-electron reduced (semiquinone), or fully reduced. Typically, the SQ form is highly unstable but can be stabilized by specific protein interactions. Cyt aa_3-600 contains a "high affinity" MQ binding site that can stabilize the SQ species, and when cyt aa_3-600 is purified, it contains 1 equiv of MQ at this site. Hence, menaquinol can reduce heme *a* in

Received: May 14, 2015
Revised: July 15, 2015
Published: July 21, 2015

DOI: 10.1021/acs.biochem.5b00528
Biochemistry 2015, 54, 5030−5044

the enzyme by one-electron and acts as a two-electron to one-electron "converter". By manipulation of the redox conditions of the solution, the paramagnetic SQ_H species can be formed at this site at concentrations that allow for characterization by EPR spectroscopy.[6]

The UQ_8 bound at the Q_H site of the homologous *E. coli* cyt bo_3, which shares high sequence identity with *B. subtilis* cyt aa_3-600, also forms a stable SQ_H when the protein is partially reduced.[7,8] X-ray crystallography, site-directed mutagenesis, and EPR methods have been used to define the residues at the cyt bo_3 Q_H-site and show details of the interactions between these residues and the bound SQ_H.[9−20] Four polar residues have been implicated in binding to the SQ at the Q_H-site in cyt bo_3: Arg-71, Asp-75, His-98, and Gln-101. In the *B. subtilis* cyt aa_3-600, the corresponding four residues at the putative Q_H site are Arg-70, Asp-74, His-94, and Glu-97 (Figure S1, see Supporting Information). Gln-101 is totally conserved in sequences from proteobacteria but is often replaced by a glutamic acid in the homologues in the Firmicutes, including the *B. subtilis* cyt aa_3-600 menaquinol oxidase.

The SQ_H species stabilized by cyt bo_3 and cyt aa_3-600 have been examined in detail using pulsed EPR methods.[6,13−20] Clearly, the SQ_H species in both cyt aa_3-600 and cyt bo_3 each exhibit a high degree of asymmetry in hydrogen bonding to the SQ: two strong H-bonds on O1 from the carbonyl adjacent to the isoprenyl group (for comparison purposes ubiquinone numbering is used in this work) and weaker interactions with O4. Both semiquinones form hydrogen bonds with nitrogen donors from arginine and histidine residues at their respective high affinity quinone binding sites. Nevertheless, isotropic hfi couplings of the nitrogen nuclei surrounding the SQ_H species indicate that the spin density transfer onto the arginine residue is weaker in cyt aa_3-600 than in cyt bo_3. In addition, the SQ_H in cyt aa_3-600 is more anionic than in cyt bo_3 because the strongest stabilizing H-bond in cyt aa_3-600 has less covalent character than the corresponding H-bond in cyt bo_3. Thus, the results show a distinctly different pattern of hydrogen bonding between the protein environments and SQ_H species in these two enzymes.

In this work, it is shown that the weaker hydrogen bonding deduced for the SQ_H species in the menaquinol oxidase correlates with greater plasticity of the site. Specifically, whereas the R71H mutant in cyt bo_3 is inactive and does not stabilize the SQ,[10] the corresponding R70H mutant in cyt aa_3-600 remains functional and does stabilize the SQ species. The mutation retains catalytic function despite the considerable disruption of the hydrogen bond network between the protein and SQ species in cyt aa_3-600. These data also provide the first direct evidence that R70 of subunit I in cyt aa_3-600 is hydrogen bonded to the menasemiquinone at the high affinity site.

EXPERIMENTAL PROCEDURES

Template Plasmid Containing the His_6-Tagged Enzyme. The template plasmid prepared in the previous study[6] was used to make mutants of the enzyme. This recombinant plasmid contained the *qoxABCD* operon (~4 kbp) cloned with the forward primer 5′-GCATAACAAAGTACTAGTTAAGGAGGGAGGAAGT**ATG**CAC-3′ (*qoxA Spe*I) and the reverse primer 5′-GAAGAGGGTTTGGGCCCTTATTCGTTATGGCCTGAATGC-3′ (*qoxD Apa*I) from genomic DNA of strain 1A1 (*B. subtilis*).

A sequence encoding for a RBS was added in the forward primer, 8 bp upstream from the start codon, and was retained within the DNA reading frame of the fragment upon the restriction digestion. The original primer set contained restriction sites *Spe*I and *Apa*I, and these were designed with the purpose of inserting DNA fragments into the expression plasmid pLala.[21] These sites are not indicated on the map of pLala (5146 bp) in the communication by Lewin et al.;[21] the restriction site *Spe*I occurs upstream of a *Bam*HI site, and *Apa*I occurs downstream of a *Cla*I site.

Previously, a His_6-tag was introduced at the C terminus of qoxB or subunit II by the PCR method of splicing by overlap extension,[22] which utilizes three separate PCR reactions in series. This method required two sets of primers, an external set encompassing the entire sequence length of aa_3-600 oxidase and an internal set containing the codons coding for six histidine residues. First, a PCR reaction was performed with pairing of an external forward primer (*qoxA Spe*I) and an internal reverse His-tag primer 5′-CCTGATCAAATA**TCA**ATGGTGATGGTGATGGTGTTCTTCTGTATC-3′. This reaction gave an ~3000 base pair DNA fragment, which was checked on a 1% DNA agarose gel and subsequently extracted and cleaned by QIAquick PCR purification kit (Qiagen). Another PCR reaction involved the pairing of an external reverse primer (*qoxD Apa*I) and an internal forward His-tag primer 5′-CAGAAGAACACCATCACCATCACCAT**TGA**TATTGATCAGG-3′. This reaction resulted in an ~1 kbp DNA fragment, which was handled as described above. Each of the two fragments of DNA had one external end of the overall construct (qoxAB-His_6CD) and an overlap region that contained a six histidine coding sequence. The final PCR reaction conducted with these two different DNA fragments and the external set of primers (*qoxA Spe*I and *qoxD Apa*I) yielded a full length sequence that incorporated a His_6-tag at the C-terminus of qoxB.

Histidine Mutation Inserted at R70 Subunit I. The forward primer 5′-GCTGTAATTATGTTATTC**CAT**GGCGGTGTCGACGGTC-3′ and the reverse primer 5′-GACCGTCGACACCGCC**ATG**GAATAACATAATTACAGC-3′ were used to insert histidine at the R70 position. The single amino acid mutation reactions were performed with QuikChange XL site-directed mutagenesis kit (Agilent, Santa Clara, CA) using the pLala aa_3-600 recombinant plasmid as the template. The resulting PCR reaction was initially treated with *Dpn*I (NEB) to digest parent dsDNA and then transformed into XL1B electrocompetent cells (*E. coli*). XL10-Gold ultracompetent cells, which are included in the QuikChange kit, are not appropriate for transformation because this strain does not allow selection by chloramphenicol. The new recombinant plasmid with the desired amino acid mutation was verified by DNA sequencing (UIUC Core Sequencing, Urbana, IL). Next, these new recombinant plasmids were transformed into strain Lu143 (*B. subtilis*), whose competent cells were prepared by a protocol involving a medium formula with Spizizen salts, 20% casamino acids, 5×LB, 50% glucose, and 5 mg/mL tryptophan. Subsequently, resulting colonies were checked for correct single mutations in *B. subtilis* by DNA sequencing. This latter step required disruption of cell pellets with 2 mg/mL lysozyme (Sigma, St. Louis, MO), which was followed by isolation of the plasmids with the Qiagen Mini-prep kit.

Steady-State Activity Assay. Previous reports of enzyme activity show variations depending on the preparative protocol, the substrate used, and the assay method.[2−4,23] The protocol in the current work is a variation of a previously reported protocol.[6] Activity was measured spectrophotometrically in a

DOI: 10.1021/acs.biochem.5b00528
Biochemistry 2015, 54, 5030−5044

coupled-enzyme assay, where the coupling enzyme, diaphorase, was used to generate reduced quinone substrate from NADH. This approach avoided the need for preparing reduced quinones prior to setting up the enzyme reaction. Each enzyme reaction volume contained the following: diaphorase in excess amount sufficient to sustain cyt aa_3-600 activity, 100 μM NADH, dimethylnitrosamine (DMN) as substrate (usually 50 μM), 0.05 μM enzyme in 50 mM Tris, 0.05% diaminodiphenylmethane (DDM), pH 6.8 buffer. The respiratory activity was started by reducing DMN in the presence of 100−200 μM NADH and an excess of purified diaphorase. To this preparation, 0.05 μM cyt aa_3-600 oxidase was added. The reaction was repeated as a function of DMN concentration in order to determine the Michaelis−Menten values. The steady-state activity was monitored by oxidation of NADH at 340 nm with an HP Agilent UV/vis spectrophotometer. Assay conditions were adjusted to minimize the background due to the autoxidation of DMN. Baseline correction due to DMN autoxidation was less than 10% of the enzymatic rate of oxygen consumption or quinol oxidation under standard assay conditions and was often negligible. At more alkaline pH values (e.g., pH 8), autoxidation was more significant, making these measurements less accurate. DT-diaphorase used in the assay was overexpressed from an *E. coli* strain, which was kindly provided by Prof. G. Cecchini's Group (UCSF). The assay performed with diaphorase from the commercially supplied strain *Clostridium kluyveri* (Sigma, St. Louis, MO) gave little or no activity in the conditions that were specified. The greatest source of variation in the results of the assays was from using different batches of diaphorase.

EPR Sample Preparation. Cells were grown in the natural abundance of ^{14}N in LB medium for unlabeled and D_2O buffer exchanged samples. For uniformly ^{15}N labeled samples, the expression strain was grown in minimal medium made with Spizizen salts and supplemented with 1 g of NH_4Cl (^{15}N, 99%) per 500 mL (Cambridge Isotope, Andover, MA). To 500 mL of minimal medium in a 2 L beveled culture flask, the following components were added to achieve high cell density: 300 μL of 20% casamino acids, 10 mL of 50% glucose (w/v), 4 mL of 5 mg/mL tryptophan, and 4 mL of 100× trace metals.[24] Each 500 mL culture was inoculated with 4 mL of overnight subculture (37 °C) and was induced with 4 mL of 50% glycerol (v/v) at the beginning. The cell culture was grown slowly for 11 h at 37 °C. The protein expression levels were lower for cultures grown on minimal medium in comparison to those prepared in LB, and generally 6 L of culture was required to prepare an isotopically labeled EPR sample.

The final buffer condition for EPR samples consisted of 100 mM Tris, 10 mM EDTA, 10% glycerol, and 0.05% DDM, pH 8.1−8.2, with an enzyme concentration of ∼200 μM. The protein samples were concentrated and buffer exchanged using Amicon centrifugal filters (Millipore, Bedford, MA). The semiquinone was generated with NADH, as described previously.

EPR Measurements. CW EPR measurements were performed at a microwave frequency of 9 GHz (X-band) with a Varian EPR-E122 spectrometer. The X- and Q-band pulsed EPR experiments were performed using a Bruker ELEXSYS E580 spectrometer equipped with an Oxford CF 935 cryostat. Field-swept two-pulse ($\pi/2-\tau-\pi-\tau$−echo) echo-detected EPR spectra were acquired to determine field positions to be used for subsequent pulse experiments. One- and two-dimensional three-pulse ($\pi/2-\tau-\pi/2-T-\pi/2$−echo) and four-pulse ($\pi/2-\tau-\pi/2-t_1-\pi-t_2-\tau$−echo) experiments were carried out as described in the previous work.[15]

Spectral processing of three- and four-pulse ESEEM was performed using the Bruker WIN-EPR software. The procedure included subtraction of the relaxation decay (fitting by 3−6° polynomials), apodization (Hamming window), zero filling, and fast Fourier transformation. For pulsed ENDOR experiments, the Davies ($\pi-t-\pi/2-\tau-\pi-\tau$−echo) sequence was used, where a radio frequency (π-pulse) was introduced during time t. The details of these experiments are discussed elsewhere.[25,26]

Spectral Simulations. ESEEM and ENDOR simulations and their fits to the experimental data were performed in the **g**-tensor frame of SQ_H with EasySpin v4.5.5 in Matlab R2013b.[27] The **g**-tensor principal axes are expected to be approximately collinear with the SQ molecular axes, based on DFT calculations and single-crystal EPR studies.[28,29] The principal axes of the hfi and nqi tensors for a histidine nitrogen interacting with the SQ carbonyl oxygen are described in relation to the **g**-tensor axes by Euler angles (α, β, γ), as defined by the EasySpin program (http://www.easyspin.org).

In this work, we use X- and Q-band pulsed EPR with microwave frequencies ∼9.7 and ∼34 GHz, respectively. At X-band, the SQ **g**-tensor anisotropy is comparable to the microwave pulse bandwidth, so pulses can be considered as giving a uniform excitation of the electron spins in the sample. Therefore, ideal strong pulses were assumed for all X-band simulations. On the other hand, at Q-band the principal components of the SQ **g**-tensor are partially resolved, allowing for orientation selective measurements by exciting only one section of the EPR spectrum at a time. In order to implement this orientation selectivity into Q-band pulsed EPR simulations, the EPR broadening of the two-pulse field swept echo and the excitation bandwidth of the pulses must be included as additional parameters. The EPR broadening was estimated by modeling the two-pulse field swept echo line width with the EasySpin H-Strain parameter. The excitation bandwidth of the pulses was approximated by multiplying the inverse of the initial microwave π-pulse by two for Davies ENDOR. For ESEEM, the excitation bandwidth was optimized during the simulation process. The combined knowledge from selective (Q-band) and nonselective (X-band) methods can provide an accurate estimate of the principal values and directions of the magnetic interactions with the SQ.

All X- and Q-band ^{14,15}N spectra were simulated together in order to obtain a more reliable estimate of the coupling constants. The simulation parameters were thus judged by their ability to reproduce all experimental spectra, as opposed to just one. The principal values and Euler angles of the hfi and nqi tensors, the pulse excitation bandwidth for ESEEM, the ENDOR line width parameter (lwENDOR in EasySpin), and the distribution of isotropic couplings ("*a*-strain", described later) were varied in the simulations. Davies suppression was incorporated into the ^{15}N ENDOR simulations as discussed previously.[26] All other settings were the same as those used in the experiments. Least-squares optimization of the simulations to the experimental spectra, where utilized, was performed iteratively until no improvement in the fit could be observed.

The ^{15}N Davies ENDOR spectra reported here were found to have low frequency peaks that were significantly weaker in intensity compared with the corresponding high frequency peaks. This deviation from the expectation of an ^{15}N doublet of symmetric ENDOR lines with approximately similar intensities

DOI: 10.1021/acs.biochem.5b00528
Biochemistry 2015, 54, 5030−5044

is due to our radio frequency generator that does not supply a constant power output over the frequency range 2−9 MHz. Hence, the simulations considered only the high frequency peaks.

DFT Calculations. The DFT calculations were performed using the B3LYP functional and the EPR-II basis set using procedures previously described.[20] All calculations were performed using the Gaussian 09 electronic structure program.[30]

Powder ^{1}H and ^{15}N ESEEM and ENDOR Spectra. The high-resolution pulsed EPR techniques, ESEEM and ENDOR, can be used to explore in detail the influence of the environment on the electronic structure of the SQ through the geometry of H-bonds and substituents, via the isotropic and anisotropic hfi with magnetic nuclei such as ^{1}H and ^{15}N.[31,32] For a hyperfine coupled ^{1}H and ^{15}N nucleus with nuclear spin $I = 1/2$, there are only two transitions with frequencies ν_α and ν_β, corresponding to the two different spin states, $m_S = \pm 1/2$, of the SQ electron spin in a constant applied magnetic field. The values of these frequencies depend on the vector sum of the applied magnetic field and the local magnetic field induced at the nucleus by the isotropic and anisotropic hfi with the electron spin.

For a powder spectrum, the frequencies of the ν_α and ν_β transitions span the range between

$$\nu_{\alpha(\beta)\perp} = |\nu_I \pm A_\perp/2| \quad \text{and} \quad \nu_{\alpha(\beta)\parallel} = |\nu_I \pm A_\parallel/2| \tag{1}$$

which correspond to the perpendicular and parallel orientations of the axial hfi tensor, respectively, ν_I is the Zeeman frequency of ^{1}H (ν_{1H}) or ^{15}N (ν^{15}_N) in the applied magnetic field, and $A_\perp = |a - T|$ and $A_\parallel = |a + 2T|$ (where a and T are the isotropic and anisotropic hyperfine coupling constants, respectively). The full axial hfi tensor has principal components $(a - T, a - T, a + 2T)$. The principal values for a rhombic hfi tensor are defined as $(a - T(1 + \delta), a - T(1 - \delta), a + 2T)$ where δ is the rhombic parameter (which ranges in value from 0 to 1).

Powder HYSCORE spectra of $I = 1/2$ nuclei reveal, in the form of cross-ridges, the interdependence of ν_α and ν_β at a given orientation.[32] The two coordinates of the cross-ridge can be used for a first-order estimate of the hyperfine coupling by taking the difference of the nuclear transitions from opposite spin manifolds ($\nu_\alpha - \nu_\beta$). This method for approximating the hfi also applies for weak couplings in powder ENDOR spectra.

Powder ^{14}N ESEEM Spectra. Because of the $I = 1$ spin and the nqi resulting from this, an ^{14}N nucleus can produce up to six lines in an ESEEM spectrum, three for each of the two electron spin manifolds, $m_S = \pm 1/2$. In measurements of amorphous (powder) samples, such as the frozen suspensions of protein used in this work, not all transitions contribute equally to the spectrum due to different orientation dependences. The ESEEM spectrum expected from ^{14}N with a predominantly isotropic hfi coupling is governed by the ratio between the effective nuclear frequency in each manifold, $\nu_{ef\pm} = |\nu^{14}_N \pm |A(^{14}N)|/2|$, and the quadrupole coupling constant, $K = e^2qQ/(4h)$.[33,34]

If $\nu_{ef-}/K \approx 0$, that is, $\nu_{ef-} \approx 0$ (the situation known as the cancellation condition, because $\nu^{14}_N \approx A(^{14}N)/2$), the three nuclear frequencies from this manifold will be close to the three pure (zero-field) nuclear quadrupole resonance frequencies with ^{14}N transitions

$$\nu_+ = K(3 + \eta) \quad \nu_- = K(3 - \eta) \quad \nu_0 = 2K\eta \tag{2}$$

and with the energy levels defined by the principal values of the nqi tensor

$$Q_{min} = -K(1 - \eta) \quad Q_{mid} = -K(1 + \eta) \quad Q_{max} = 2K \tag{3}$$

Both eq 2 and eq 3 are completely described by K and the asymmetry parameter η. These frequencies, with the property $\nu_+ = \nu_- + \nu_0$, are broadened as $\nu_{ef\pm}/K$ departs from 0 but can appear in the spectrum up to a ratio of $\nu_{ef\pm}/K \approx 0.75-1$.[33,34]

A three-pulse ESEEM spectrum near the cancellation condition is expected to consist of four lines: three narrow lines at zero-field nqi frequencies from the manifold with $\nu_{ef-} \approx 0$, eq 2, and one broadened double-quantum transition ν_{dq+} from the opposite manifold, described by the relationship

$$\nu_{dq\pm} = 2[\nu_{ef\pm}{}^2 + K^2(3 + \eta^2)]^{1/2} \tag{4}$$

Since ν_{dq+} is from the manifold not satisfying the cancellation condition, it may be too broad to observe in the three-pulse ESEEM spectrum. However, the corresponding HYSCORE spectrum will exhibit cross-peaks correlating ν_+, ν_-, and ν_0 with ν_{dq+}, indicating the location of ν_{dq+} even if it is not directly observed. The cross-peak contour line shapes are expected to be narrow ridges parallel to one coordinate axis and perpendicular to the other. The narrowness of the cross-peaks in one dimension over the other reflects the sharpness of lines near the cancellation condition (ν_+, ν_-, and ν_0) as opposed to the nuclear transition not satisfying the cancellation condition (ν_{dq+}). The total number of possible cross-peaks from one nitrogen in each quadrant is nine pairs.[35] On the other hand, when the nitrogen coupling is far from the cancellation condition, the HYSCORE spectrum is expected to simplify into that of a single pair of cross-peaks correlating the double-quantum transitions from opposite spin manifolds (ν_{dq+} and ν_{dq-}).

RESULTS

Steady-State Activity. By the protocol described in the Experimental Procedures section, the steady state activity at pH 6.8 using reduced DMN as the substrate yielded values of k_{cat} and K_M for the wild-type enzyme of 180 DMN/s and 89 μM DMN and for the R70H mutant of 227 DMN/s and 55 μM DMN with approximately 10% error in multiple assays performed on the same day with the same enzyme preparation. Assays performed with different batches of diaphorase on different days gave results that varied considerably (±30% from a mean value). Nevertheless, under the same conditions, the R70H mutant is always more active than the wild-type enzyme. The steady-state activity was measured over the range of pH 6 to pH 9, and the change observed at pH 6.8 is not due to a shift in the pH-activity profile, which is not substantially altered by the R70H mutation.

EPR Spectra. X-band CW EPR spectra of the SQ_H in WT cyt aa_3-600 along with the R70H mutant (Figure S2) display a similar pattern with a g value of 2.0047 ± 0.0001 and resolved hfi structure consisting of four components with approximate relative intensities 1:3:3:1 and splittings of 0.45−0.49 mT (or 12−13 MHz). The structure is better resolved for the samples prepared in $^{2}H_2O$. On the other hand, uniform ^{15}N labeling of the protein does not significantly influence the EPR line-shape of the SQ_H. Based on previous work with the WT protein,[6] this EPR feature is tentatively assigned to the three equivalent

DOI: 10.1021/acs.biochem.5b00528
Biochemistry 2015, 54, 5030−5044

nonexchangeable protons of the semiquinone ring methyl group interacting with the unpaired electron spin.

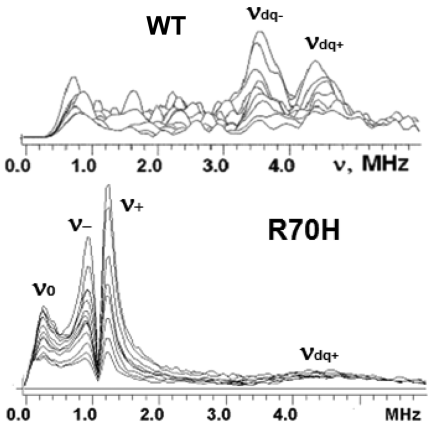

Figure 1. Comparison of the X-band ^{14}N three-pulse ESEEM spectra of wild-type cyt aa_3-600 and the R70H mutant. The spectra were recorded as a function of time, τ, between the first and second pulses at the field position corresponding to the maximum EPR intensity for SQ_H in the WT and R70H cyt aa_3-600. Three lines at low frequencies (0.25, 0.99, and 1.24 MHz) in the spectrum of the mutant indicate ^{14}N with a quadrupole coupling constant K = 0.37 MHz, which is typical of a protonated histidine nitrogen (see Table 3).

Nitrogens Interacting with the SQ_H as Detected by 1D and 2D ESEEM in Wild-Type and Mutant Protein. Figure 1 shows stacked plots of the three-pulse ESEEM spectra of SQ_H in the WT and R70H cyt aa_3-600 from 0 to 6 MHz, appropriate for the ^{14}N nucleus. The three-pulse ESEEM spectrum of the WT protein contains only two lines at frequencies 3.5 and 4.4 MHz and does not resolve any other features. These frequencies are correlated in the 2D ESEEM spectrum as belonging to the same nitrogen with a hfi coupling of ~0.9 MHz.[6] This nitrogen is tentatively assigned to N_ε of R70 based on the estimated $K^2(3 + \eta^2)$ value, which is similar to that determined for N_ε of R71 in cyt bo_3.[13,16] In the case of cyt bo_3, this assignment was directly confirmed using selective ^{15}N labeling of the nitrogens in the arginine residue.[17]

In contrast, the three-pulse spectrum of SQ_H in the R70H mutant has a shape typical for a single ^{14}N recorded near cancellation conditions and allows for an immediate assignment of the narrow peaks at ~0.25, 0.99, and 1.24 MHz to three nuclear quadrupole resonance frequencies ν_0, ν_-, and ν_+ with the property $\nu_0 + \nu_- = \nu_+$ (see eq 2). There is also a much weaker and broader line at ~4−5 MHz, which can be suggested to belong to the ν_{dq+} transition (see eq 4). This assignment was confirmed by the ^{14}N HYSCORE spectrum (Figure 2). The spectrum exhibits cross-peaks correlating ν_0, ν_-, and ν_+ with ν_{dq+}, thus indicating that they belong to different electron spin manifolds. They also allow for a more precise determination of the value of $\nu_{dq+} \approx 4.3–4.7$ MHz from the maximum intensity of the (ν_{dq+}, ν_+) cross-correlation.

Having obtained the frequencies for ν_0, ν_-, ν_+, and ν_{dq+}, eqs 2 and 4 along with the ^{14}N Zeeman frequency (ν^{14}_N = 1.06 MHz) were used to determine the qcc K = 0.37 MHz, the asymmetry parameter η = 0.32, and the hfi coupling $A(^{14}N)$ = 2.18 MHz for the nitrogen nucleus.

The Q-band ^{14}N HYSCORE spectrum of SQ_H in R70H cyt aa_3-600 shows one intensive pair of cross-peaks **1** in the (++) quadrant at (9.9, 5.3) MHz (Figure S3). The ^{14}N Zeeman

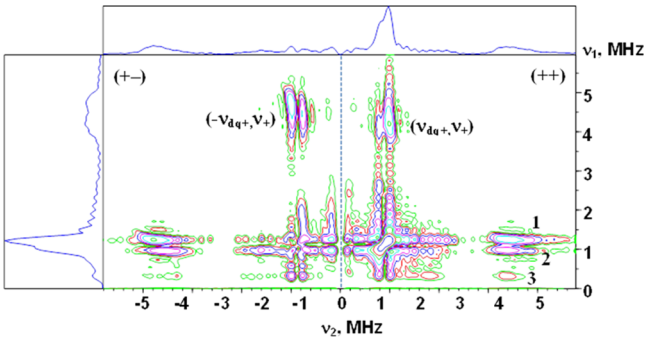

Figure 2. Contour representation of the X-band ^{14}N HYSCORE spectrum of SQ_H in R70H cyt aa_3-600. Numbers define the following cross-peaks: 1, (ν_+, ν_{dq+}); 2, (ν_-, ν_{dq+}); 3, (ν_0, ν_{dq+}). Experimental parameters: magnetic field 344.4 mT, time between first and second pulses τ = 136 ns, microwave frequency 9.659 GHz, temperature 80 K, step Δt = 20 ns.

frequency in this experiment was 3.75 MHz (1218.7 mT) giving ν_{ef-}/K = 7 and ν_{ef+}/K = 13, thus indicating that the observed cross-peaks correlate dq-transitions from opposite manifolds. These frequencies provide an estimate of the hfi coupling $A(^{14}N) \approx 2.3$ MHz in good agreement with the value determined from the X-band spectra.

In summary, the ^{14}N spectra of SQ_H in the R70H mutant cyt aa_3-600 oxidase resolve an interaction with only a single nitrogen (N1) possessing significant presumably isotropic hfi coupling resulting from the transfer of unpaired spin density from the SQ via a hydrogen bond bridge. The value of K characterizes the chemical type of the ^{14}N nucleus interacting with the SQ_H, which is typical for a protonated nitrogen of an imidazole residue (see Table 3 below).

X-Band ^{15}N HYSCORE. The ^{14}N ESEEM spectra do not resolve any lines from other side-chain and peptide nitrogens of the nearby protein environment. These nitrogens are coupled more weakly and do not produce well-defined lines in the ^{14}N powder-type spectra, due to the influence of the nqi. However, the lines from weakly coupled nitrogens (N_{wc}) can be observed in 2D ^{15}N ESEEM spectra, which are not complicated by the nqi, as shown in our previous experiments with cyt bo_3 and wild-type cyt aa_3-600.[6,17,20] Furthermore, ^{15}N spectra allow for a more precise determination of the isotropic and anisotropic components of the hfi tensor of the nitrogen nuclei.

The X-band ^{15}N HYSCORE spectrum for SQ_H in ^{15}N uniformly labeled R70H cyt aa_3-600 is shown in Figure 3. The spectrum contains cross-features **1** and **1′**, located in the (+−) and (++) quadrants, with maxima at (−3.1, 0.2) MHz (**1**) and (2.8, 0.3) MHz (**1′**). The first-order estimates of the hyperfine couplings are 3.3 and 3.1 MHz, respectively (2.4 and 2.2 MHz when scaled to ^{14}N). These values are consistent with the coupling estimated from the ^{14}N HYSCORE spectra.

In addition, the (++) quadrant exhibits feature $\mathbf{N_{wc}}$ with a maximum near the diagonal point (ν^{15}_N, ν^{15}_N) and accompanying shoulders symmetrically extended up to ~1 MHz along the antidiagonal (Figure 3). Two resolved splittings, ~0.4 MHz ($\mathbf{1_{wc}}$) and ~0.8 MHz ($\mathbf{2_{wc}}$), can be suggested from an analysis of the shoulders' line shape. The $\mathbf{N_{wc}}$ features result from multiple nonequivalent contributions of weakly coupled ^{15}N nuclei in the immediate vicinity of SQ_H. Comparison of the $\mathbf{N_{wc}}$ line shape with the previously published data for SQ_H in the WT and D75H cyt bo_3[20] reveals unique characteristics for each spectrum that reflect differences in the protein environment.

DOI: 10.1021/acs.biochem.5b00528
Biochemistry 2015, 54, 5030−5044

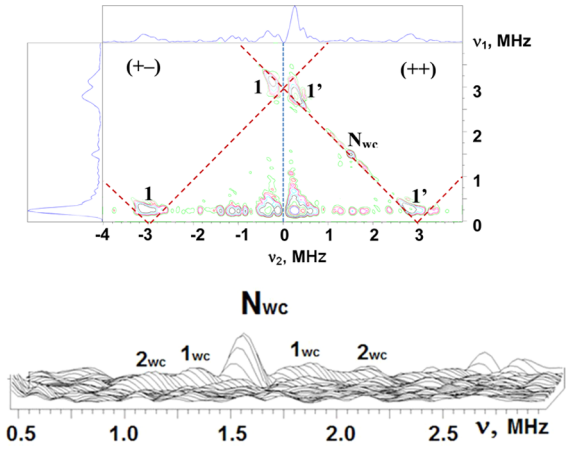

Figure 3. Contour (top) presentation of the ^{15}N HYSCORE spectrum of SQ_H in ^{15}N uniformly labeled R70H cyt aa_3-600. Stacked (bottom) presentation of the $\mathbf{N_{wc}}$ feature in the (++) quadrant of the spectrum. Stacked presentation of the full spectrum is shown in Figure S4. The red dashed straight line segments in the contour representation are defined by $|\nu_1 \pm \nu_2| = 2(\nu^{15}_N)$. Experimental parameters: magnetic field 343.25 mT, time between first and second pulses τ = 136 ns, microwave frequency 9.625 GHz, temperature 60 K.

To further resolve the individual interactions with the nitrogens in the SQ_H environment, selective ^{15}N labeling of individual residues needs to be employed.

Simulations of the X-Band ^{15}N HYSCORE Spectrum: "*a*-Strain" Influence on Cross-Peak Line Shape. Appearance of the cross-peaks **1** and **1′** with comparable intensity in the (++) and (+−) quadrants from the same nucleus suggests that the special relationship $|2a + T| \approx 4\nu^{15}_N$ is closely fulfilled. The case $|2a + T| = 4\nu^{15}_N$ is well-known in powder 1D ESEEM where $\nu_{\beta(\alpha)\perp} = -\nu_{\beta(\alpha)\parallel} = \pm(3T/4)$ (S singularity).[36] Under this condition, all orientations contribute to the same frequency $|3T/4|$, resulting in a singularity for the nuclear transition from one manifold. In 2D spectra, the theoretically predicted line shape corresponding to the S-singularity becomes a straight line segment parallel to the $\nu_{\alpha(\beta)}$ axis in the interval from $\nu_{\alpha(\beta)\perp} = |a - T/4|$ to $\nu_{\alpha(\beta)\parallel} = |a + 5T/4|$ at $\nu_{\beta(\alpha)} = |3T/4|$.[37] However, in contrast to this expectation, the cross-features in both quadrants of the experimental spectrum contain a straight part parallel to the ν_1 or ν_2 axis to good accuracy as well as a second component of the ridge extending along the antidiagonal into the (+−) and (++) quadrants. As a result, the cross-peaks in both quadrants exhibit a curvature not in accordance with the theoretically predicted line shape for a single I = 1/2 anisotropic hfi.[37,38]

The X-band ^{15}N HYSCORE spectrum provides an opportunity for a simple separate estimate of the isotropic and anisotropic hfi couplings for the strongly coupled nitrogen N1. Model simulations show that comparable intensity of the cross-peaks in the (++) and (+−) quadrants is observed only in a very narrow interval around the condition $|2a + T| = 4\nu^{15}_N$. Exploiting this relation and value of the frequency $\nu = 3T/4 \sim 0.25 - 0.3$ MHz for the straight segment parallel to the $\nu_{1(2)}$ axis, one can estimate $a^{14}_N \approx 2.05$ MHz, $T^{14}_N \approx 0.2$ MHz (recalculated for ^{14}N). The powder type X-band ^{15}N HYSCORE spectrum simulated with these parameters (Figure S5) shows coincidence of the simulations with the segments of the cross-peaks parallel to the ν_1 or ν_2 axes but does not reproduce the total curved shape of the cross-peaks extending along the blue dashed antidiagonal line.

The experimentally observed line shapes were reproduced under the assumption of a significant distribution of isotropic hfi couplings, that is, "*a*-strain", resulting from fluctuations in the protein environment.[39−41] The *a*-strain was incorporated into the simulations under the assumption of a Gaussian distribution for *a*. This was performed by simulating multiple HYSCORE spectra over a range of values for *a*, weighting the relative intensities of each spectrum to a Gaussian distribution, and then summing all of the spectra together. Figure S5 shows example spectra calculated using this method for different standard deviations σ. According to these calculations, an increase in the width of the distribution leads to a longer extension of the cross-ridge along the antidiagonal. The best agreement with the experiment was obtained for σ^{15}_N = 0.35 MHz (σ^{14}_N = 0.25 MHz) (Figure 4). This distribution of the isotropic coupling is used in the simulations of all other spectra considered in this work.

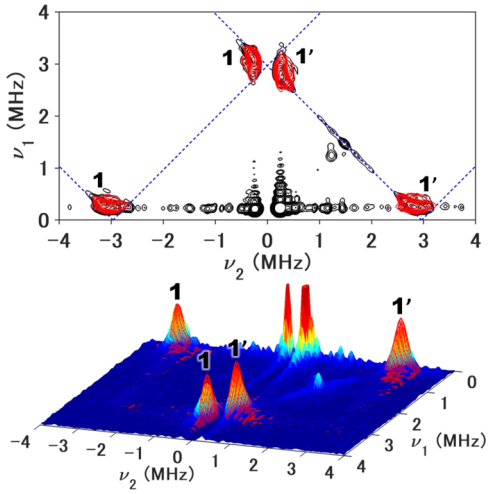

Figure 4. Comparison of the experimental X-band ^{15}N HYSCORE spectrum of SQ_H and its simulation employing a Gaussian distribution $f(\Delta a) = [\sigma(2\pi)^{1/2}]^{-1} \exp[-(\Delta a)^2/(2\sigma^2)]$ for the isotropic hyperfine coupling with standard deviation σ^{15}_N = 0.35 (σ^{14}_N = 0.25) MHz. Spectra are presented in contour (top) and stacked (bottom) modes. Simulation of features **1** and **1′** is shown in red. The dashed lines in the contour representation are defined by $|\nu_1 \pm \nu_2| = 2(\nu^{15}_N)$. Experimental parameters are as in Figure 3. Examples of spectra calculated with other values for the standard deviation are presented in Figure S5.

Q-Band ^{15}N ENDOR and HYSCORE. We collected orientation-selective Q-band Davies ^{15}N ENDOR spectra in order to obtain information about the principal directions of the hfi tensor in the **g**-tensor coordinate system for the strongly coupled nitrogen N1. Q-band (~34 GHz) measurements on SQ_H were performed at a frequency (field) range 3−4 times higher than X-band that leads to an increase of the EPR line width of SQ_H up to ~3.0 mT and allows one to carry out orientation selective measurements by exciting different sections of the EPR spectrum.

Q-band Davies ENDOR was acquired at seven evenly spaced field positions spanning the full field swept two-pulse echo (Figure 5). Despite the poor resolution of the g_X, g_Y, and g_Z components in the field swept echo, an orientation dependence in the Davies ENDOR spectrum is observed, especially at orientations near g_Z. The Davies ENDOR spectra in Figure 5

DOI: 10.1021/acs.biochem.5b00528
Biochemistry 2015, 54, 5030−5044

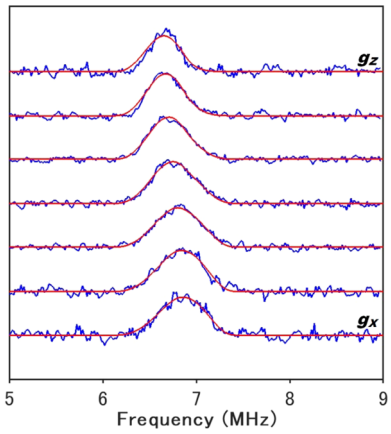

Figure 5. Q-band ^{15}N Davies ENDOR spectra of SQ_H. Only the high-frequency component of the ^{15}N spectrum is shown. Traces were taken at seven field positions from 1218.5 mT (bottom trace, g_X) to 1221.3 mT (top trace, g_Z) in steps of 0.4 mT. The experimental data are shown in blue and are overlaid by the simulations in red. Simulations of Q-band spectra were performed using the g-values 2.00644, 2.00526, and 2.00298 with H-Strain line width broadenings 22, 35, and 40 MHz, respectively. Experimental parameters: microwave $\pi/2$-pulse length 120 ns, time between first and second pulses τ = 500 ns, RF π-pulse length 70 μs, microwave frequency 34.249 GHz, temperature 60 K, $\nu_{^{15}N}$ = 5.26 MHz.

show only a single resolvable splitting with an average hfi coupling of ~3.0 (2.1 for ^{14}N) MHz.

In agreement with these observations, increasing the microwave frequency to Q-band (leading to significant deviation from singularities and cancellation for N1) greatly simplifies the shape of the cross-peaks in the ^{15}N HYSCORE spectra to that of a simple doublet in the (++) quadrant (Figure S6) with the frequency coordinates consistent with the maxima of the lines in the Q-band ENDOR spectra.

Determination of the Hfi and Nqi Tensors from Spectral Simulations. Davies ENDOR simulations were performed using the a-strain parameter estimated from the X-band calculations (σ^{15}_N = 0.35 MHz) without any assumptions about the principal values and directions of the hfi tensor. As a consequence of implementing a distribution for a, however, the simulations became strongly insensitive to the choice of rhombicity factor δ. While a least-squares optimization of the Davies ENDOR spectra at various fixed values of δ suggested a weak preference for a more axial tensor (δ = 0), the resulting fits were not statistically different enough to provide a reliable estimate for δ. Therefore, δ was left undetermined and set to zero so as to reduce the number of free parameters in the calculations. The ENDOR simulations (Figure 5) were optimized by adjusting the hfi coupling constants iteratively by hand, and then were fine-tuned by least-squares minimization.

The initial values for K and η were determined from the analysis of Figure 1 under the assumption of near cancellation for the coupled nitrogen. Simulations of the three-pulse ^{14}N ESEEM (Figure S7) alongside the Q-band ^{14}N HYSCORE spectra (Figure S3), as well as the ^{15}N ENDOR and HYSCORE spectra (Figures 4,5, and S6), were done iteratively until a parameter set was obtained that could reproduce the general features of all of the experimental data considered. It should be noted that substantially better agreement of the simulations with the experimental spectra was achieved with the inclusion of the a-strain determined above in all cases (especially for the X-band ^{15}N HYSCORE spectrum). The principal values and orientations of the principal axes of the hfi and nqi tensors of N1 in the **g**-tensor coordinate system are summarized in Table 1.

Table 1. ^{14}N Hyperfine and Nuclear Quadrupole Tensor Simulation Parameters[a]

hyperfine tensor	a = 2.0 ± 0.1 MHz
	T = 0.2 ± 0.1 MHz
	δ = 0[b]
	β = 90° ± 20°
	γ = 30° ± 20°
nuclear quadrupole tensor	K = 0.36 ± 0.02 MHz
	η = 0.25 ± 0.05 MHz
	α = 110° ± 40°
	β = 60° ± 180°
	γ = 100° ± 40°

[a]The hfi (a, T, δ) and nqi (K, η) coupling constants are defined in the text, and the Euler angles (α, β, γ) are defined in accordance with the EasySpin standard as the series of rotations necessary to go from the hfi/nqi eigenframe into the **g**-tensor frame. [b]The simulations were insensitive to δ, so the value was fixed as zero. For an axial tensor, α does not need to be defined.

Proton HYSCORE and ESEEM. Besides the nitrogens, the HYSCORE spectra contain information about nonexchangeable and exchangeable protons interacting with the electron spin of the SQ_H. Figure 6 shows the ^{1}H HYSCORE spectra of the SQ_H in R70H cyt aa_3-600 prepared in ^1H_2O (see also spectrum in Figure S8). Similar spectra for the SQ_H in cyt bo_3 and cyt aa_3-600 have been discussed previously.[6,15,16] In addition to a diagonal peak at the proton Zeeman frequency (ν_{1H}, ν_{1H}) (ν_{1H} ≈ 14.7 MHz), the spectrum contains several pairs of resolved cross-features located symmetrically relative to the diagonal. They are designated $\mathbf{1}_H$, $\mathbf{2}_H$, $\mathbf{3}_H$, $\mathbf{4}_H$ and $\mathbf{4'}_H$, $\mathbf{5}_H$ and $\mathbf{5'}_H$, and $\mathbf{6}_H$. Cross-peaks $\mathbf{2}_H$, $\mathbf{3}_H$, $\mathbf{4}_H$ and $\mathbf{4'}_H$, and $\mathbf{5}_H$ and $\mathbf{5'}_H$ completely disappear in the HYSCORE spectra obtained under the same conditions when the sample is prepared in D_2O (Figure S9), showing that they are produced by exchangeable protons. However, cross-peaks $\mathbf{1}_H$ and $\mathbf{6}_H$, as well as the diagonal peak, still appear in the spectra obtained in D_2O. The H/D exchange does affect the intensity of cross-peaks $\mathbf{6}_H$, thus indicating the simultaneous contribution of exchangeable and nonexchangeable protons. Additional support for this conclusion was obtained from pulsed ENDOR spectra (Figure S11).

The cross-peaks $\mathbf{1}_H$ from nonexchangeable proton(s) possess the largest hfi splitting, of the order ~11−12 MHz, and can be tentatively assigned to the protons of the methyl group stemming from the quinone ring (see Figure 8) based on our previous studies of cyt bo_3 and its mutants and cyt aa_3-600.[6,15,16] From the spectral features of the exchangeable protons, one can reasonably suggest that the extended ridges $\mathbf{2}_H$, $\mathbf{3}_H$, and $\mathbf{4}_H$ belong to three unique protons based on differences in the deviation of the cross-ridges from the antidiagonal passing through (ν_{1H}, ν_{1H}). On the other hand, the identity of $\mathbf{3'}_H$, $\mathbf{4'}_H$, and $\mathbf{5}_H$ is not clear but can be tested via linear regression of ridges $\mathbf{2}_H$−$\mathbf{4}_H$ in ν_1^2 vs ν_2^2 coordinates. Linear regressions of $\mathbf{2}_H$, $\mathbf{3}_H$, and $\mathbf{4}_H$ are shown in Figure S10. Extension of the linear fit of $\mathbf{2}_H$ crosses $\mathbf{4'}_H$ but its orientation is not coincident with the line defined by $\mathbf{2}_H$. Moreover, the linear

DOI: 10.1021/acs.biochem.5b00528
Biochemistry 2015, 54, 5030−5044

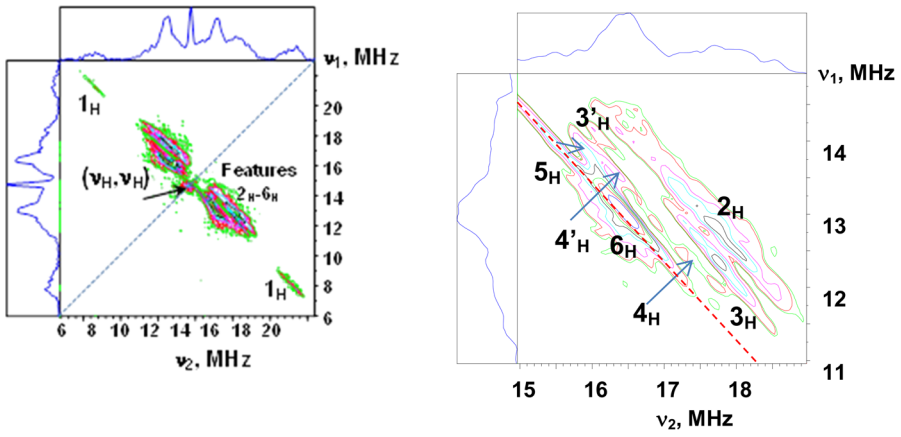

Figure 6. ^{1}H HYSCORE spectrum of the SQ_H from R70H cyt aa_3-600 in a $^{1}H_2O$ buffer. The full presentation (left) and an enhanced view of features $\mathbf{2_H}$–$\mathbf{6_H}$ (right) are shown. The spectrum was obtained after Fourier transformation of the two-dimensional time-domain patterns containing 256 points × 256 points with a 20 ns step. The magnetic field was 345.25 mT, time τ between the first and second microwave pulses was 200 ns, and the microwave frequency was 9.680 GHz.

extrapolation of $\mathbf{3_H}$ coincides well with the $\mathbf{3'_H}$ and $\mathbf{5_H}$ segments, suggesting that these features belong to the same extended ridge. The remaining features $\mathbf{4_H}$ and $\mathbf{4'_H}$ align reasonably well by linear regression, although part of the low intensity $\mathbf{4_H}$ ridge deviates substantially from the straight line, which may be explained by the influence of FT artifacts accompanying the intensive $\mathbf{6_H}$ peak.

Quantitative analysis of the cross-ridge contour line shapes in ν_1^2 vs ν_2^2 coordinates[37,38] and simulations of the Davies pulsed ENDOR spectra, described in Supporting Information (see Figures S10, S12, and S13 and Table S1), provide the isotropic and anisotropic components of the hfi tensors under an axial approximation for protons H1–H4. The data are summarized in Table 2. Cross-peaks $\mathbf{6_H}$ are produced by several

Table 2. ^{1}H Hyperfine Tensors Determined from HYSCORE Spectra of the SQ_H in R70H cyt aa_3-600 in H_2O[a]

proton	cross-ridges	a_1 (MHz)	a_2 (MHz)	T (MHz)
H1	$\mathbf{1_H}$	12.8	−14.4	1.5
H2	$\mathbf{2_H}$	0.7	−6.3	5.6
H3	$\mathbf{3_H}$-$\mathbf{3_H'}$-$\mathbf{5_H}$	0.7	−5.3	4.5
H4	$\mathbf{4_H}$-$\mathbf{4_H'}$	0.5	−4.0	3.5

[a]Selection of the isotropic couplings for methyl and exchangeable protons is based on analysis of pulsed ENDOR spectra (Figure S8) and DFT calculations.

nonexchangeable and weakly coupled exchangeable protons (see Discussion), and the parameters determined from their formal analysis would not correspond to any real structural characteristics.

Additional support for the hfi tensors of the exchangeable protons reported above was obtained from the complementary one-dimensional four-pulse ESEEM spectra.[42] Similarly, these spectra show the existence of three exchangeable protons with anisotropic couplings $T \approx 5.6$, 4.5, and 3.4 MHz (Figure S14 and Supporting Information).

DISCUSSION

Summary of Cyt bo_3 Studies. Our initial studies of cyt bo_3 were extended to cyt aa_3-600 in order to decipher the differences between the protein–quinol interactions of the bo_3-type ubiquinol oxidase and the aa_3-600 menaquinol oxidase. Four polar residues have been implicated in binding to the quinol at the Q_H site in cyt bo_3: R71, D75, H98, and Q101. Q101 is replaced by a glutamic acid (E97) in the *B. subtilis* aa_3-600 menaquinol oxidase (Figure S1). The nitrogen H-bond donors around the SQ_H in cyt bo_3 were identified unambiguously by selective ^{15}N labeling of particular amino acids using auxotrophic hosts.[17,20] A set of auxotrophs was constructed in a commonly used *E. coli* expression strain C43(DE3) for isotopic labeling of individual amino acids or sets of amino acids.[17,20,43] These auxotrophs were used to generate WT and D75H cyt bo_3 samples with specific nitrogens of the arginine, histidine, or glutamine residues ^{15}N labeled. Two-dimensional ESEEM has identified N_ε of R71 in cyt bo_3 and N_ε of H75 in the D75H mutant as the H-bond donors carrying the most unpaired spin density transferred from the SQ_H of UQ_8. In addition, weak hfi couplings with the side-chain and peptide nitrogens from R71, H98, and Q101 were resolved, thus obtaining a full view of the spin density transfer from the SQ_H to the nearest residues in both enzymes. Use of the 2D technique was crucial for observation of these weak signals, which are masked by more intensive lines in the 1D spectra.

Available ^{1}H (H-bonds, methyl),[15,16] ^{13}C (methyl),[19] and ^{15}N (protein)[17,20] couplings in both WT and D75H enzymes were interpreted with the assistance of DFT calculations on model complexes.[20] In the absence of accurate data from the X-ray crystal structure, idealized small models of the SQ_H–protein interactions with geometry optimization were explored. This work indicates strong H-bonds in the WT protein between O1 and both D75 and the N_ε of R71, but a much weaker H-bond to the N_ε-H group of H98 to O4. The result is a highly asymmetric distribution of the unpaired spin density, which appears to be an important factor to optimize electron transfer between the SQ_H and the heme *b* electron acceptor during catalytic turnover. The replacement of the carboxyl of D75 by the imidazole in D75H leads to a weaker H-bond to O1 and a significantly smaller hyperfine coupling between the SQ_H and R71 than that in WT. The computations indicate that this is due to a change in the geometry of the H-bond rather than a change in bond length. The end result is a more symmetric distribution of the unpaired spin density in the UQ ring in the mutant, which may correlate with lack of catalysis.

Nitrogen Interactions in Cyt aa_3-600 and R70H Mutant. The 2D ESEEM studies found a significant difference

DOI: 10.1021/acs.biochem.5b00528
Biochemistry 2015, 54, 5030–5044

Table 3. Hfi and Nqi Coupling Constants for Histidines Hydrogen Bonded to Semiquinones[a]

quinone site	H residue	$a(^{14}N)$ (MHz)	4K (MHz)	η	quinone	ref
Q_A *Sphaeroides*	M219 N_δ	2.3	1.50	0.97	UQ_{10}	26
Q_A *Viridis*	M217 N_δ	~ 2	1.51	0.87	MQ_9	44
Q_B *Sphaeroides*	L190 N_δ	1.3−1.4	1.50−1.54	0.69	UQ_{10}	45
Q_D NarGHI	66 N_δ	0.8	1.96	0.5	MQ_8	46
Q_A PSII	214 N_δ	1.67−1.9	1.47−1.58	0.71−0.78	PQ_9	47, 48
Q_i bc_1	217 N_ε	0.75	1.44	0.17	UQ_{10}	49
Q_H D75H bo_3	75 N_ε	2.5	1.72	0.73	UQ_8	16, 20
Q_H R70H aa_3	70 N_ε	2	1.44	0.25	MQ_7	this work

[a]Currently available data from the literature are shown in the Table. Only nqi tensors determined from three-pulse ESEEM spectra with at least one resolvable single-quantum transition are shown, so as to consider only the most accurate determinations of η. The coupling constants listed in the table vary within ~25−30% range for e^2qQ/h, a factor of ~3 for $a(^{14}N)$, and a factor of ~5 for η.

between the SQs of UQ_8 in cyt bo_3 and MQ_7 in cyt aa_3-600. ^{14}N and ^{15}N ESEEM experiments were performed with the SQ_H in WT cyt aa_3-600 containing natural abundance ^{14}N and with uniformly ^{15}N-labeled protein.[6] ^{14}N spectra revealed a nitrogen with hfi coupling $A(^{14}N)$ = 0.94 MHz and nqi parameter $\kappa = K^2(3 + \eta^2)$ = 2.7 MHz^2. For the SQ_H in the WT cyt bo_3 the $N_\varepsilon H$ of R71 possesses the largest hfi coupling $A(^{14}N) \approx$ 1.8 MHz and an nqi tensor with K = 0.93 MHz and η = 0.51.[13,16] These values give κ = 2.82 MHz^2, which differs only slightly from the estimated value of κ = 2.7 MHz^2 for the nitrogen from cyt aa_3-600. This close coincidence of the nqi parameter κ suggests that the N_ε of R70 in cyt aa_3-600 also takes on the role of the nitrogen carrying the largest unpaired spin density and, thus, is involved in H-bond formation with the SQ_H. The ^{15}N HYSCORE spectrum exhibits extended shoulders with two resolved maxima corresponding to couplings of 0.96 and 0.4 MHz, respectively. It is likely that the ^{15}N line shape with two resolved splittings is formed by the spectra from several (probably more than two) nitrogens that are partially overlapped.

Mutagenesis of the conserved arginine at the Q_H site indicates a significant difference between cyt bo_3 and cyt aa_3-600. In particular, converting R71 (*B. subtilis* R70) to histidine is lethal for the *E. coli* oxidase,[10] but the same mutant in *B. subtilis* cyt aa_3-600 is more active than the wild-type. Our X-band 1D and 2D ESEEM experiments with the R70H mutant show the formation of a H-bond between the SQ and histidine nitrogen possessing the qcc K = 0.36 MHz, typical for protonated nitrogens of an imidazole ring. The isotropic coupling $a(^{14}N) \approx$ 2 MHz of this nitrogen exceeds the couplings in the WT and is comparable to the largest couplings in WT cyt bo_3 (1.8 MHz) and D75H mutant (2.7 MHz).[16] In addition, ^{15}N X- and Q-band HYSCORE spectra of R70H clearly show the presence of nitrogen(s) with weaker couplings of ~0.5 MHz. These weakly coupled nitrogens, as well as the nitrogen donors in WT cyt aa_3-600, are not yet identified. Our attempts to express the *B. subtilis* cyt aa_3-600 in an *E. coli* expression system have failed. Therefore, we cannot utilize *E. coli* auxotroph strains[43] for selective isotopic labeling of these proteins. Instead, the interpretation and assignment of ^1H and $^{14,15}N$ data are based on the results of our DFT calculations discussed below.

N_δ vs N_ε. Our X- and Q-band ESEEM/ENDOR experiments with the SQ_H in the R70H mutant of cyt aa_3-600 have established an interaction with a nitrogen possessing a significant ~2 MHz isotropic hfi coupling. This hfi coupling strength exceeds those found previously in the WT protein. The qcc of this nitrogen is consistent with the constants reported for the ^{14}N histidine nitrogens hydrogen bonded with the SQ in other quinone processing sites (Table 3). Therefore, we conclude that the largest unpaired spin density in the R70H mutant is transferred through hydrogen bonding with the histidine nitrogen.

From a comparative analysis of the hfi and nqi tensor characteristics for the histidine N_δ H-bond donors of SQs in different quinone sites from Table 3 in our previous publication,[26] we found a remarkably good linear correlation between the isotropic hfi constant $a(^{14}N)$ and the asymmetry parameter η (Figure 7). In contrast to N_δ, two points in the

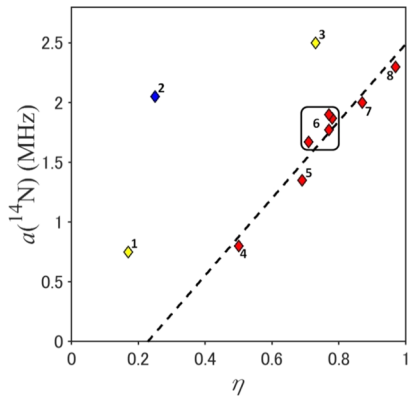

Figure 7. Correlation between $a(^{14}N)$ and η is demonstrated for the semiquinone−histidine complex data in Table 3. Red diamonds, N_δ of Q_A *Rb. sphaeroides* (8), Q_A *Rp. viridis* (7), Q_A PSII (6), Q_B *Rb. sphaeroides* (5), Q_D NarGHI (4); yellow diamonds, N_ε of Q_i cyt bc_1 (1) and Q_H D75H cyt bo_3 (3). The blue diamond represents data obtained for Q_H cyt aa_3-600 in this work.

graph of a vs. η corresponding to hydrogen bonded N_ε in the Q_i site of the bc_1 complex and Q_H site of D75H mutant of cyt bo_3 significantly deviate from the linear plot.

The point corresponding to the H-bonded nitrogen in the R70H mutant also deviates significantly from the linear plot. This suggests that the identity of the H-bond donor from H70 to SQ_H is the N_ε. Previous studies of the D75H cyt bo_3 mutant have shown that in addition to H75, H98 is also involved in weak H-bonding with the oxygen from the opposite carbonyl through N_ε. Taking into account the similarity of the Q_H sites, one can suggest that N_ε of H94 is also H-bonded in WT and R70H cyt aa_3-600.[20] This H-bond would lead to the appearance of the isotropic coupling with the N_ε of the order ~0.5 MHz.

DOI: 10.1021/acs.biochem.5b00528
Biochemistry 2015, 54, 5030−5044

Exchangeable Protons. Analysis of the 1D and 2D ^{1}H ESEEM spectra of SQ_H in the R70H cyt aa_3-600 indicates three protons with the anisotropic hfi constants $T \approx 5.6$, 4.5, and 3.5 MHz. In contrast, two exchangeable protons with $T \approx 5.6$ and 2.9 MHz were resolved in the spectra of the WT protein.[6] One can note that deviation of the cross-ridges from the antidiagonal (ν_{1H}, ν_{1H}) and the shift of the sum-combinations from $2\nu_{1H}$ for $T \leq 2.9$ MHz are close to the resolution limits defined by the individual width of the spectral lines. Therefore, one cannot exclude the possible existence of at least one more proton with a similar value $T \approx 2.9$ MHz in the WT cyt aa_3-600. Protons H-bonded with different SQs in frozen water and alcohol solutions possess the typical value $T \approx 2.6$–2.9 MHz.[50−52] Hydrogen bonding to the SQ carbonyl groups occurs via proton donation to the two lone pairs on the sp^2-hybridized carbonyl oxygen. DFT calculations show that a hfi coupling of $|T| \approx 3$ MHz is consistent for a proton participating in a planar hydrogen bond, forming an angle 60° with the C═O bond, and with a H-bond length ∼1.8 Å.[53] A similar bond length can be estimated using a point-dipole model for the O···H bond.

It is reasonable to propose that the H-bond(s) to the SQ_H of cyt aa_3-600 involving the proton with $|T| \approx 2.9$ MHz, are close to this geometry. The second exchangeable proton detected in cyt aa_3-600 has a much larger anisotropic coupling, $|T| \sim 5.6$ MHz that suggests a H-bond with the proton located within a shorter distance of the SQ's oxygen. However, the point-dipole approximation becomes inappropriate for O···H distances $R <$ 1.7 Å with $T >$ 3.5 MHz, as follows from model DFT calculations,[53] and the value $T \approx 5.6$ MHz would correspond to the distance ∼1.3 Å, implying a substantial covalent character for the O−H bond. Comparison of these data with hfi couplings for the exchangeable protons in the R70H mutant indicates that the appearance of histidine instead of arginine retains the largest hfi coupling 5.6 MHz and increases the strength of two other couplings up to 4.5 and 3.5 MHz relative to the value 2.9 MHz in the WT protein.

For comparison, 2D ESEEM spectra of the SQ_H in cyt bo_3 show several cross-peaks sensitive to D_2O buffer exchange.[15] Analysis of these cross-peaks indicates two protons with large anisotropic hfi (∼4.2 and 6.3 MHz) assigned to the protons interacting with carbonyl oxygens. The pulsed EPR experiments were extended using two mutants at the Q_H site.[16] The D75E mutation has little influence on the catalytic activity, and the pattern of hydrogen bonding was similar to the WT with two exchangeable proton signals possessing $T \approx 4.7$ MHz. In contrast, in the inactive D75H mutant, only one exchangeable proton with $T \approx 4.6$ MHz was found. In addition, a signal with $T \approx 1.5$ MHz was observed in all these samples and assigned to other weakly coupled exchangeable protons around the SQ.

Hyperfine Coupling for Methyl Protons and Asymmetry in Spin Density Distribution. Available experimental data for Q sites indicate that the local environment modifies the electronic state of the SQ in each protein, influencing the distribution of the unpaired spin density. In proteins, it is usually asymmetric, in contrast to frozen solutions.[31,32]

A simple quantitative measure of the asymmetry in the spin density distribution can be obtained from the ^{1}H couplings of the methyl group in UQs or 3-methyl-1,4-naphthoquinones (see Figure 8). The isotropic hfi constant for the methyl protons of the SQ varies within 5.5−6.0 MHz in UQs and from 7.0 to 7.9 MHz in 3-methyl-1,4-naphthoquinone derivatives in liquid and solid organic solvents (see Table 2 in ref 6).

In contrast to these results, the isotropic constant varies significantly in proteins (Table 4). The coupling $a \approx$ 10−11 MHz was found for the methyl protons of SQ_H in cyt bo_3 and cyt aa_3-600 and the A_1 center of the PS I.[6,15,59,60] The couplings ∼8−9 MHz in D75E and D75H mutants are still 1.5 times the values in alcohol solutions.[51] By comparison, the SQ_H in the R70H mutant possesses the largest value of the isotropic coupling for the methyl protons of 12.8 MHz, though an increase of the coupling relative to the corresponding value in frozen solution is still slightly higher for UQ in cyt bo_3 (1.85 ± 0.15) than for MQ in R70H (1.7 ± 0.1). The asymmetrical H-bonding pattern exhibited by the SQ in these proteins is the opposite of that found for the SQ_A in the bacterial RC from *Rb. sphaeroides*. The isotropic coupling of the methyl protons is ∼4.5−5.0 MHz in the SQ_A, that is, smaller than that of an anion radical in solution and consistent with the stronger hydrogen bond donation to the O4 oxygen than the O1 oxygen.[31] In addition, the methyl protons for the SQ of the MQ-9 in the Q_A site of the RC from *Rhodopseudomonas viridis* have an isotropic constant that is not quite as large, ∼6.8 MHz.[61] This is even smaller, 5.5 MHz, for MQ-8 in NarGHI.[62] These data suggest the same explanation as for SQ_A above. In contrast, the stronger hydrogen bond donation to the O1 oxygen explains the large methyl couplings in cyt bo_3, cyt aa_3-600, and PS I.

Table 4. Comparison of Experimental and Calculated ^{1}H Isotropic Hfi Couplings for Methyl Protons of the Semiquinones in Selected Q Sites

site	quinone	a_{exp}, MHz	a_{calc}, MHz	ref
Q_A RC	UQ-10	4.5−5.0	4.3	54[a]
				31, 55[b]
Q_B RC	UQ-10	5.4−5.8	5.8	56[a]
				31, 57[b]
A_1 PS I	phylloquinone	9.8−9.94	9.4	58[a]
				59, 60[b]
Q_H cyt bo_3	UQ-8	10−11	9.2	20[a]
				15[b]
Q_H D75H cyt bo_3	UQ-8	8.0	8.2	20[a]
				16[b]
Q_H cyt aa_3	MQ-7	11.0	14.1 (10.0)	this work,[a] 6[b]
Q_H R70H cyt aa_3	MQ-7	12.8	10.4	this work

[a]Computational publication. [b]Experimental publication.

In the cases discussed above, several nonequivalent hydrogen bonds are formed between the SQ oxygens and protein residues. A cumulative effect resulting from the common influence of H-bonds of different geometries and strengths leads to the asymmetrical redistribution of unpaired spin density in the SQ. DFT calculations taking into account all H-bonds around the SQ can provide a good model of the spin density distribution as well as an explanation for the experimentally observed hfi couplings and these are discussed below.

DFT Calculations on Model Compounds. Our models used for DFT calculations were generated using the homologous cyt bo_3 Q_H site crystal structure pdb 1FFT[9] as a starting point for the residue positions (no structure is currently available for cyt aa_3-600). The WT cyt aa_3-600 SQ_H was modeled with hydrogen bonds from the carboxylic acid OH group of D74 and the $N_\varepsilon H$ guanidium group of R70 to O1 and

DOI: 10.1021/acs.biochem.5b00528
Biochemistry 2015, 54, 5030−5044

$N_\varepsilon H$ of the imidazole group of H94 to O4. For the R70H mutant, the guanidium group representing the side chain of R70 was replaced with an imidazole group representing the histidine interaction. It should be emphasized that in the absence of accurate structural data for cyt aa_3-600, we can only explore idealized small models with full or partial geometry optimization. Therefore, it is unlikely that the correct positioning and orientation of the H-bonds with respect to SQ_H are reproduced. Nevertheless, by comparing different models, the calculated values can provide valuable insight into understanding how the EPR data reflect structural differences between WT and R70H.

The following four calculations were performed: (a) full geometry optimization of an isolated model of the SQ with no hydrogen bonding to O1 or O4, (b) full geometry optimization of the WT model described above, (c) single-point calculation of WT model in which the hydrogen bond between the O1 and the $N_\varepsilon H$ fragment of the guanidium group representing R70 was fixed at 2.5 Å with all other geometric parameters held at their fully optimized values (designated "WT-1"), and (d) full geometry optimization of an R70H mutant model in which the guanidium group representing R70 in WT is replaced by an imidazole group representing the histidine mutation.

The calculated Mülliken spin densities on the SQ ring are given in Figure 8. A symmetrical spin density distribution for

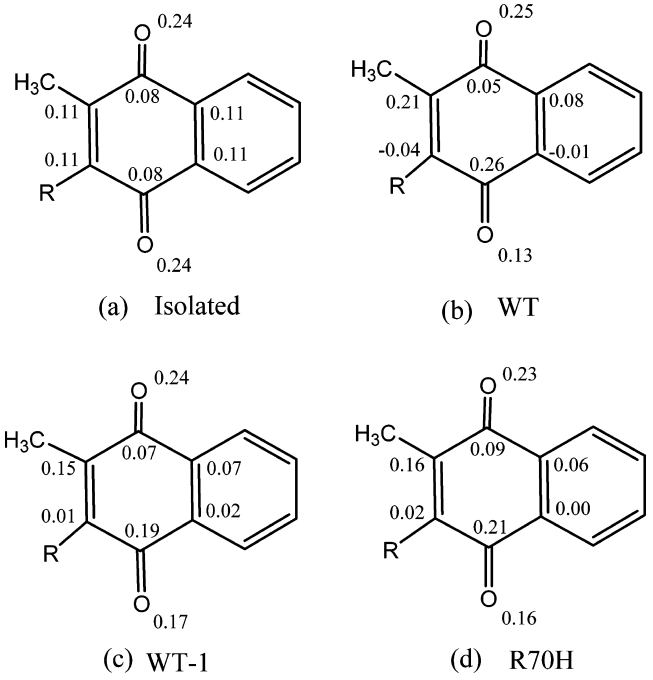

Figure 8. Calculated Mülliken spin densities for isolated, WT, and R70H mutant models. For comparison purposes ubiquinone numbering is used; bottom oxygen is O1. R is CH_3CH_2 or CH_3; no difference in spin populations are found between these substituents.

the SQ ring is displayed for the isolated model. Compared with the isolated model, the SQ_H site models show the expected polarization of spin due to stronger hydrogen bonding at the O1 oxygen. Polarization is largest for the fully optimized WT model. The modified wild-type model (WT-1), in which the hydrogen bond to R70 has been elongated, exhibits a similar polarization of spin as the R70H mutant model.

The validities of the models can be tested by comparison of the calculated ^{14}N (Table 5) and proton CH_3 (Table 6) couplings with the experimental EPR data. For the R70H model, the calculated values are in good agreement with the experiments. However, for the WT protein the extensive polarization of the SQ calculated for the fully optimized model is not supported by experimental values for either ^{14}N or CH_3. Instead, better agreement with the experimental ^{14}N and CH_3 couplings is observed using the longer 2.5 Å R70 H-bond interaction of the WT-1 model.

As described above, several exchangeable ^1H hfi couplings were identified, presumably from hydrogen bonded protons in both the WT and R70H mutant. In the case of WT, 2D ESEEM identified two protons with anisotropic constants T = 5.6 and 2.9 MHz.[6] Table 6 shows that the calculated values of T ($=T_{33}/2$) for the three hydrogen bonded protons for WT from R70, H94, and D74 are 5.2, 3.1, and 3.4 MHz, respectively. For WT-1, the corresponding calculated T values are 1.6, 3.8, and 3.4 MHz, which are in worse agreement with the experimental values than the WT model. This demonstrates the limitations of the DFT model used here without the availability of the correct crystal structure. Nevertheless, as indicated above, the WT-1 model is in better agreement with the overall spin density distribution observed experimentally, so we take this to be the better representation of the real system. For the mutant R70H, three distinct exchangeable protons having T values of 5.6, 4.5, and 3.5 MHz were determined from an analysis of the ^1H HYSCORE spectrum (Table 2). Calculated T values for our R70H model (Table 6) are 4.1, 3.3, and 3.9 MHz for H70, H94, and D75, respectively, which are in qualitative agreement with the experiment.

In summary, the DFT data show that the hydrogen bonding interaction of the MQ SQ_H with the guanidium group of the R70 residue in cyt aa_3-600 is weaker than the equivalent interaction between R71 and UQ SQ_H in cyt bo_3. This can be explained by a longer hydrogen bond formed to R70 in cyt aa_3-600. The R70H mutation in cyt aa_3-600 results in a more optimal hydrogen bond to the menaquinol O1, increasing the asymmetry of the spin density distribution in SQ_H. In contrast, the equivalent R71H mutation in cyt bo_3 forms a less optimal hydrogen bond, which precludes formation of SQ_H as well as quinol oxidase activity.[10] Although the R71H mutant of cyt bo_3 does not form a stable semiquinone,[10] the D75H mutant of cyt bo_3, which is also inactive, does form a semiquinone, which does have a more symmetrical spin density distribution based on a comparison of the ^1H methyl couplings[20] (Table 4).

Pure "*a*-Strain" Resolution in Two-Dimensional Spectra. Analysis of the EPR line width of metallocomplexes and clusters in frozen solutions and proteins has previously shown that in many cases the line width scaled approximately with the microwave frequency. It was proposed that frequency (field) dependent contributions to the line width originate from the **g**-tensor distribution. This phenomenon is more commonly referred to as "**g**-strain".[39−41] In addition to the **g**-strain, a distribution of hyperfine couplings, that is, *A*-strain, was also reported.[40] The importance of this conclusion is that any chemical structure including a protein cannot be considered uniquely trapped in a solid state but contains a distribution of structures that gives rise to **g**- and *A*-strain. However, in one-dimensional spectra, several factors usually contribute to the line width and significant efforts are needed in order to determine pure contributions from **g**- and *A*-strain.

DOI: 10.1021/acs.biochem.5b00528
Biochemistry 2015, 54, 5030−5044

Table 5. Calculated ^{14}N Isotropic Hyperfine Couplings (a_{iso}), Nuclear Quadrupole Coupling Constant (K), and the asymmetry parameter (η), for the Q_H site cyt aa_3-600 Models[a]

	WT (WT-1)				R70H		
	a_{iso}	K	η		a_{iso}	K	η
R70−N_ε	3.5 (1.0)	0.8 (1.0)	0.6 (0.3)	H70−N	1.8	0.5	0.1
R70−N_H	0.0 (1.2)	1.1 (1.1)	0.3 (0.3)				
R70−N_H	0.3 (0.3)	1.1 (1.1)	0.2 (0.3)				
H94−N	−0.5 (0.2)	0.5 (0.5)	0.1 (0.1)	H94−N	−0.6	0.5	0.2

[a] a_{iso} and K are in MHz. Values for WT-1, which denotes model with elongated hydrogen bond to R70, are given in parentheses.

Table 6. Methyl and Hydrogen Bonded ^1H Isotropic (a_{iso}) and anisotropic (T_{nn}) Hyperfine Couplings Calculated for the Q_H Site Models Described in Text[a]

	isolated		WT(WT-1)		R70H	
position	T_{33}, T_{22}, T_{11}	a_{iso}	T_{33}, T_{22}, T_{11}	a_{iso}	T_{33}, T_{22}, T_{11}	a_{iso}
CH_3	2.6	6.9	3.0 (2.7)	14.1 (10.0)	2.7	10.4 (12.8)
	−1.3		−1.5 (−1.4)		−1.4	
	−1.3		−1.5 (−1.4)		−1.4	
R70−NH_ε/H70−NH			10.3 (3.2)	−0.1 (0.0)	8.2	−0.2
			−5.6 (−1.7)		−4.3	
			−4.8 (−1.5)		−3.9	
H94−NH			6.2 (7.6)	−0.6	6.5	−0.7
			−3.4 (−3.9)		−3.7	
			−2.7 (−3.8)		−2.9	
D75−COOH			6.8 (6.8)	0.0	7.8	−0.4
			−3.6 (−3.5)		−4.0	
			−3.2 (−3.2)		−3.8	

[a] All values are given in MHz.

The hfi tensor of $^{15}N_\varepsilon$ from H70 H-bonded with the SQ_H in cyt aa_3-600 corresponds with very high accuracy to a special case satisfying the condition $|2a + T| = 4\nu^{15}_N$ ($a^{15}_N \approx 2.87$ MHz, $T^{15}_N \approx 0.28$ MHz, $\nu^{15}_N = 1.5$ MHz). In this case, one of the nuclear frequencies possesses a constant value $|3T/4|$ for all orientations of the magnetic field relative to the principal axes of the hyperfine tensor, which suggests an appearance of the cross-features in both quadrants of the 2D spectra in the form of straight line segments parallel to one of the axes. However, in contrast to this expectation, the cross-features in the experimental spectra exhibit a curvature not in accordance with the theoretically predicted line shape for a single $I = 1/2$ anisotropic hfi (Figures 3 and 4).[37,38] Theory predicts a value of frequency $|3T^{15}_N/4| \approx 0.2$ MHz only, and one can suggest that variations of the hfi coupling of the same order would give a comparable contribution to this frequency and will change the line shape of the cross-features. In agreement with this assumption, the experimentally observed cross-feature line shape was reproduced in the calculations with a distribution for the isotropic hfi coupling. Changes in a were targeted as the potential cause of the nonideal line shapes in the HYSCORE spectra, because we previously found a (but not T) to be very sensitive to the histidine−SQ hydrogen bond length, resulting in reported isotropic couplings that vary by up to a factor of ∼3 (Table 3).[26] Using a Gaussian distribution, the best agreement was obtained with a standard deviation $\sigma^{15}_N = 0.35$ MHz, that is, slightly larger than 10% of the isotropic coupling. The anisotropic coupling with the N_ε is about ten times smaller, and variations of this coupling of a similar order are of a few hundred megahertz only. This contribution has been ignored at this stage of analysis.

The isotropic coupling $a = 2.87$ MHz corresponds to 2s spin density population 1.13×10^{-3}, based on the unit spin ^{15}N atomic hfi constant $a = 2535.4$ MHz,[63] and variations of the spin density $\sim 10^{-4}$ are responsible for the observed changes of the spectral line shape. It is interesting to note that for many nonmetallic protein systems, no noticeable line broadenings due to **g**-strain effects were observed with increasing magnetic field strength. For instance, for the primary donor cation radical P in RCs from *Rb. sphaeroides*, fields up to 24 T were applied,[64] and **g**-strain broadening was found to be negligible. Similar conclusions followed from a comparison of the line widths in the EPR spectra of SQ_A and SQ_B measured from 9 GHz and up to 360 GHz.[31,57] However, in contrast to these EPR results, in addition to the findings described in this article for SQ_H, we have found the pronounced influence of a-strain on the ^{15}N HYSCORE spectra of the SQ_A in bacterial reaction centers of *Rb. sphaeroides*. The a-strain in this case is responsible for an appearance of the new lines of low intensity in the ^{15}N X-band spectra. These lines were unassigned in our previous work based on the traditional analysis of the cross-peak line shape.[26] This effect will be considered in greater detail in a separate publication.

CONCLUSION

Cyt aa_3-600 is a terminal oxidase in the electron transport pathway that contributes to the electrochemical membrane potential by actively pumping protons. A notable feature of this enzyme complex is that it uses as its electron donor menaquinol instead of cytochrome c, when it reduces dioxygen to water. The enzyme stabilizes a menasemiquinone radical (SQ) at a high affinity site Q_H that is important for catalysis. One of the residues in the Q_H site that interacts with the SQ_H is Arg70. We

DOI: 10.1021/acs.biochem.5b00528
Biochemistry 2015, 54, 5030−5044

have made the R70H mutant and have characterized the SQ_H radical by advanced EPR. X- and Q-band $^{14,15}N$ pulsed EPR data and DFT calculations show that the SQ_H interacts with the N_ε of H70 based on its quadrupole coupling constant e^2qQ/h = 1.44 MHz typical for protonated imidazole nitrogens. This nitrogen possesses a strong isotropic hyperfine coupling ($a^{14}_N \approx$ 2.0 MHz) resulting from unpaired spin density transferred from the SQ_H via a hydrogen bond bridge. This hydrogen bond replaces the H-bond with N_ε from the R70 side chain in wild-type cyt aa_3-600. The mutation also changes the number and strength of the hydrogen bonds in the SQ_H environment as determined by the analysis of the ^1H 2D ESEEM spectra. However, the R70H mutation still retains significant asymmetry in the unpaired spin density distribution as follows from the value of the ^1H methyl isotropic coupling equal to 12.8 MHz. Despite the alterations in the immediate environment of the SQ_H, the R70H remains catalytically active. This is in contrast to the equivalent mutation in the close homologue, the cyt bo_3 ubiquinol oxidase from *E. coli*, where the similar R71H mutation eliminates function.

The reasons for the different biochemical consequences of the equivalent mutations in cyt bo_3 and cyt aa_3-600 are not evident and will require further studies. There is a correlation between the enhanced menaquinol oxidase activity of the R70H mutant of cyt aa_3-600 and the increased asymmetry of the spin density distribution in the SQ_H compared with the WT. This is consistent with the effect of the D75H mutation of cyt bo_3, which forms a stable SQ_H with reduced asymmetry of the spin density distribution and which is not enzymatically active.[20] Unfortunately, the inactive R71H mutant of cyt bo_3 does not form a stable SQ_H. Recognizing the limited data, so far the experimental data supported by DFT calculations indicate a correlation between quinol oxidase activity and a strong asymmetry of the unpaired spin density distribution (and, hence, charge distribution) in the SQ_H, which is regulated by the hydrogen bond network. On the other hand, the retained (or enhanced) activity of the cyt aa_3-600 R70H mutant but not in the cyt bo_3 R71H mutant might also be due to the much lower midpoint potential of the menaquinol substrate compared with the ubiquinol substrate used with cyt bo_3. The WT cyt aa_3-600 does not utilize ubiquinol as a substrate, but further work on cyt bo_3 mutants with different substrates could help clarify how these mutations alter enzyme function. These topics could be addressed more deeply with the availability of high-resolution structures of cyt bo_3 and cyt aa_3-600. The structures would provide more precise knowledge of the quinone location in proteins and lead to a more accurate modeling of the SQ_H state in both WT proteins and mutants using magnetic resonance data reported in this and previous publications.

■ ASSOCIATED CONTENT

Supporting Information

The Supporting Information is available free of charge on the ACS Publications website at DOI: 10.1021/acs.biochem.5b00528.

Relevant methodological details and Figures S1−S14 (PDF)

■ AUTHOR INFORMATION

Corresponding Authors

*S.A.D.: e-mail, dikanov@illinois.edu; phone, (217) 300-2209.

*R.B.G.: e-mail, r-gennis@illinois.edu; phone, (217) 333-9075.

*P.J.O.: e-mail, patrick.omalley@manchester.ac.uk; phone, 00441612004536.

Present Address

[▽]A.T.T.: Department of Biochemistry and Molecular Biology, Nippon Medical School, Sendagi, Bunkyo-ku, Tokyo 113−8602, Japan.

Funding

This research was supported by Grants DE-FG02-08ER15960 (S.A.D.) and DE-FG02-87ER13716 (R.B.G.) from Chemical Sciences, Geosciences and Biosciences Division, Office of Basic Energy Sciences, Office of Sciences, US DOE, NIH Grant GM062954 (S.A.D.), and NCRR/NIH Grants S10-RR15878 and S10-RR025438 for pulsed EPR instrumentation. P.J.O. acknowledges the use of computer resources granted by the EPSRC UK national service for computational chemistry software (NSCCS). A.T.T. gratefully acknowledges support as a NIH trainee of the Molecular Biophysics Training Program (Grant 5T32-GM008276).

Notes

The authors declare no competing financial interest.

■ ABBREVIATIONS:

cyt, cytochrome; RBS, ribosomal binding site; 2D, two-dimensional; CW, continuous-wave; DFT, density functional theory; B3LYP, Becke3 Lee−Yang−Parr; SQ, semiquinone; EPR, electron paramagnetic resonance; ESEEM, electron spin echo envelope modulation; HYSCORE, hyperfine sublevel correlation; MQ_n, menaquinone-*n*; UQ_n, ubiquinone-*n*; hfi, hyperfine interaction; nqi, nuclear quadrupole interaction; qcc, quadrupole coupling constant; WT, wild-type

■ REFERENCES

(1) Winstedt, L., and von Wachenfeldt, C. (2000) Terminal oxidases of *Bacillus subtilis* strain 168: One quinol oxidase, cytochrome aa_3 or cytochrome *bd*, is required for aerobic growth. *J. Bacteriol. 182*, 6557−6564.

(2) Lauraeus, M., Haltia, T., Saraste, M., and Wikstrom, M. (1991) *Bacillus subtilis* expresses two kinds of haem-A-containing terminal oxidases. *Eur. J. Biochem. 197*, 699−705.

(3) Lemma, E., Schagger, H., and Kroger, A. (1993) The menaquinol oxidase of *Bacillus subtilis* W23. *Arch. Microbiol. 159*, 574−578.

(4) Henning, W., Vo, L., Albanese, J., and Hill, B. C. (1995) High-yield purification of cytochrome aa_3 and cytochrome caa_3 oxidases from *Bacillus subtilis* plasma membranes. *Biochem. J. 309*, 279−283.

(5) Santana, M., Kunst, F., Hullo, M. F., Rapoport, G., Danchin, A., and Glaser, P. (1992) Molecular cloning, sequencing, and physiological characterization of the *qox* operon from *Bacillus subtilis* encoding the aa_3-600 quinol oxidase. *J. Biol. Chem. 267*, 10225−10231.

(6) Yi, S. M., Narasimhulu, K. V., Samoilova, R. I., Gennis, R. B., and Dikanov, S. A. (2010) Characterization of the semiquinone radical stabilized by the cytochrome aa_3-600 menaquinol oxidase of *Bacillus subtilis*. *J. Biol. Chem. 285*, 18241−18251.

(7) Ingledew, W. J., Ohnishi, T., and Salerno, J. C. (1995) Studies on a stabilisation of ubisemiquinone by *Escherichia coli* quinol oxidase, cytochrome *bo*. *Eur. J. Biochem. 227*, 903−908.

(8) Sato-Watanabe, M., Itoh, S., Mogi, T., Matsuura, K., Miyoshi, H., and Anraku, Y. (1995) Stabilization of a semiquinone radical at the high-affinity quinone-binding Site (Q_H) of the *Escherichia coli bo*-type ubiquinol oxidase. *FEBS Lett. 374*, 265−269.

(9) Abramson, J., Riistama, S., Larsson, G., Jasaitis, A., Svensson-Ek, M., Laakkonen, L., Puustinen, A., Iwata, S., and Wikström, M. (2000) The Structure of the ubiquinol oxidase from *Escherichia coli* and its ubiquinone binding site. *Nat. Struct. Biol. 7*, 910−917.

DOI: 10.1021/acs.biochem.5b00528
Biochemistry 2015, 54, 5030−5044

(10) Hellwig, P., Yano, T., Ohnishi, T., and Gennis, R. B. (2002) Identification of the residues involved in stabilization of the semiquinone radical in the high-affinity ubiquinone binding site in cytochrome bo_3 from *Escherichia coli* by site-directed mutagenesis and EPR Spectroscopy. *Biochemistry 41*, 10675−10679.
(11) Veselov, A. V., Osborne, J. P., Gennis, R. B., and Scholes, C. P. (2000) Q-band ENDOR (Electron Nuclear Double Resonance) of the high-affinity ubisemiquinone center in cytochrome bo_3 from *Escherichia coli*. *Biochemistry 39*, 3169−3175.
(12) Hastings, S., Heathcote, P., Ingledew, W. J., and Rigby, S. E. J. (2000) ENDOR spectroscopic studies of stable semiquinone radicals bound to the *Escherichia coli* cytochrome bo_3 quinol oxidase. *Eur. J. Biochem. 267*, 5638−5645.
(13) Grimaldi, S., Ostermann, T., Weiden, N., Mogi, T., Miyoshi, H., Ludwig, B., Michel, H., Prisner, T., and MacMillan, F. (2003) Asymmetric binding of the high-affinity Q_H^- ubisemiquinone in quinol oxidase (bo_3) from *Escherichia coli* studied by multifrequency Electron Paramagnetic Resonance spectroscopy. *Biochemistry 42*, 5632−5639.
(14) Grimaldi, S., MacMillan, F., Ostermann, T., Ludwig, B., Michel, H., and Prisner, T. (2001) Q_H-ubisemiquinone radical in the bo_3-type ubiquinol oxidase studied by pulsed Electron Paramagnetic Resonance and Hyperfine Sublevel Correlation Spectroscopy. *Biochemistry 40*, 1037−1043.
(15) Yap, L. L., Samoilova, R. I., Gennis, R. B., and Dikanov, S. A. (2006) Characterization of the exchangeable protons in the immediate vicinity of the semiquinone radical at the Q_H Site of the cytochrome bo_3 from *Escherichia coli*. *J. Biol. Chem. 281*, 16879−16887.
(16) Yap, L. L., Samoilova, R. I., Gennis, R. B., and Dikanov, S. A. (2007) Characterization of mutants that change the hydrogen bonding of the semiquinone radical at the Q_H site of the cytochrome bo_3 from *Escherichia coli*. *J. Biol. Chem. 282*, 8777−8785.
(17) Lin, M. T., Samoilova, R. I., Gennis, R. B., and Dikanov, S. A. (2008) Identification of the nitrogen donor hydrogen bonded with the semiquinone at the Q_H site of the cytochrome bo_3 from *Escherichia coli*. *J. Am. Chem. Soc. 130*, 15768−15769.
(18) MacMillan, F., Kacprzak, S., Hellwig, P., Grimaldi, S., Michel, H., and Kaupp, M. (2011) Elucidating mechanisms in haem copper oxidases: The high-affinity Q_H binding site in quinol oxidase as studied by DONUT-HYSCORE spectroscopy and density functional theory. *Faraday Discuss. 148*, 315−344.
(19) Lin, M. T., Shubin, A. A., Samoilova, R. I., Narasimhulu, K. V., Baldansuren, A., Gennis, R. B., and Dikanov, S. A. (2011) Exploring by pulsed EPR the electronic structure of ubisemiquinone bound at the Q_H site of cytochrome bo_3 from *Escherichia coli* with in vivo ^{13}C-labeled methyl and methoxy substituents. *J. Biol. Chem. 286*, 10105−10114.
(20) Lin, M. T., Baldansuren, A., Hart, R., Samoilova, R. I., Narasimhulu, K. V., Yap, L. L., Choi, S. K., O'Malley, P. J., Gennis, R. B., and Dikanov, S. A. (2012) Interactions of intermediate semiquinone with surrounding protein residues at the Q_H site of the wild type and D75H mutant cytochrome bo_3 from *Escherichia coli*. *Biochemistry 51*, 3827−3838.
(21) Lewin, A., Su, X.-D., and Hederstedt, L. (2009) Positively regulated glycerol/G3P-dependent *Bacillus subtilis* gene expression system based on anti-termination. *J. Mol. Microbiol. Biotechnol. 17*, 61−70.
(22) Rumbley, J. N., Nickels, E. F., and Gennis, R. B. (1997) One-step purification of histidine-tagged cytochrome bo_3 from *Escherichia coli* and demonstration that associated quinone is not required for the structural integrity of the oxidase. *Biochim. Biophys. Acta, Protein Struct. Mol. Enzymol. 1340*, 131−142.
(23) Mattatall, N. R., Cameron, L. M., and Hill, B. C. (2001) Transient-state reduction and steady-state kinetic studies of menaquinol oxidase from Bacillus subtilis, cytochrome aa_3-600. Spectroscopic characterization of the steady-state species. *Biochemistry 40*, 13331−13341.
(24) Harwood, C. R., and Cutting, S. M. (1990) *Molecular Biological Methods in Bacillus*, 618 pp, Wiley & Sons, Ltd., West Sussex, England.
(25) Schweiger, A., and Jeschke, G. (2001) *Principles of Pulse Electron Paramagnetic Resonance*, Chapter 12, Oxford University Press, Oxford, U.K.
(26) Taguchi, A. T., O'Malley, P. J., Wraight, C. A., and Dikanov, S. A. (2014) Hyperfine and nuclear quadrupole tensors of nitrogen donors in the Q_A site of bacterial reaction centers: Correlation of the histidine N_δ tensors with hydrogen bond strength. *J. Phys. Chem. B 118*, 9225−9237.
(27) Stoll, S., and Britt, R. D. (2009) General and efficient simulation of Pulse EPR spectra. *Phys. Chem. Chem. Phys. 11*, 6614−6625.
(28) Taguchi, A. T., O'Malley, P. J., Wraight, C. A., and Dikanov, S. A. (2015) Hydrogen bond network around the semiquinone of the secondary quinone acceptor Q_B in bacterial photosynthetic reaction centers. *J. Phys. Chem. B 119*, 5805−5814.
(29) Isaacson, R. A., Lendzian, F., Abresch, E. C., Lubitz, W., and Feher, G. (1995) Electronic structure of Q_A^- in reaction centers from *Rhodobacter sphaeroides*. I. Electron Paramagnetic Resonance in single crystals. *Biophys. J. 69*, 311−322.
(30) Frisch, M. J., Trucks, G. W., Schlegel, H. B., Scuseria, G. E., Robb, M. A., Cheeseman, J. R., Scalmani, G., Barone, V., Mennucci, B., Petersson, G. A., Nakatsuji, H., Caricato, M., Li, X., Hratchian, H. P., Izmaylov, A. F., Bloino, J., Zheng, G., Sonnenberg, J. L., Hada, M., Ehara, M., Toyota, K., Fukuda, R., Hasegawa, J., Ishida, M., Nakajima, T., Honda, Y., Kitao, O., Nakai, H., Vreven, T., Montgomery, J. A., Jr., Peralta, J. E., Ogliaro, F., Bearpark, M., Heyd, J. J., Brothers, E., Kudin, K. N., Staroverov, V. N., Kobayashi, R., Normand, J., Raghavachari, K., Rendell, A., Burant, J. C., Iyengar, S. S., Tomasi, J., Cossi, M., Rega, N., Millam, J. M., Klene, M., Knox, J. E., Cross, J. B., Bakken, V., Adamo, C., Jaramillo, J., Gomperts, R., Stratmann, R. E., Yazyev, O., Austin, A. J., Cammi, R., Pomelli, C., Ochterski, J. W., Martin, R. L., Morokuma, K., Zakrzewski, V. G., Voth, G. A., Salvador, P., Dannenberg, J. J., Dapprich, S., Daniels, A. D., Farkas, O., Foresman, J. B., Ortiz, J. V., Cioslowski, J., and Fox, D. J. (2009) *Gaussian 09*, revision A.1, Gaussian, Inc., Wallingford CT.
(31) Lubitz, W., and Feher, G. (1999) The primary and secondary acceptors in bacterial photosynthesis. III. Characterization of the quinone radicals Q_A and Q_B by EPR and ENDOR. *Appl. Magn. Reson. 17*, 1−48.
(32) Dikanov, S. A. (2013) Resolving Protein-Semiquinone Interactions by Two-Dimensional ESEEM Spectroscopy. *Electron Paramagn. Reson. 23*, 103−179.
(33) Dikanov, S. A., Tsvetkov, Y. D., Bowman, M. K., and Astashkin, A. V. (1982) Parameters of quadrupole coupling of ^{14}N nuclei of chlorophyll *a* cations determined by Electron Spin Echo method. *Chem. Phys. Lett. 90*, 149−153.
(34) Flanagan, H., and Singel, D. J. (1987) Analysis of ^{14}N ESEEM patterns of randomly oriented solids. *J. Chem. Phys. 87*, 5606−5616.
(35) Dikanov, S. A., Xun, L., Karpiel, A. B., Tyryshkin, A. M., and Bowman, M. K. (1996) The orientationally-selected two-dimensional ESEEM spectroscopy of the Rieske-type iron-sulfur cluster in 2,4,5-Trichlorophenoxyacetate monooxygenase from *Burkholderia cepacia* AC1100. *J. Am. Chem. Soc. 118*, 8408−8416.
(36) Lai, A., Flanagan, H., and Singel, D. J. (1988) Multifrequency electron spin echo envelope modulation in S = 1/2, I = 1/2 systems: Analysis of spectral ampltudes, line shapes and line widths. *J. Chem. Phys. 89*, 7161−7166.
(37) Dikanov, S. A., and Bowman, M. K. (1995) Cross-peak lineshape of two-dimensional ESEEM spectra in disordered $S = 1/2$, $I = 1/2$ spin systems. *J. Magn. Reson., Ser. A 116*, 125−128.
(38) Dikanov, S. A., Tyryshkin, A. M., and Bowman, M. K. (2000) Intensity of cross-peaks in HYSCORE spectra of $S = 1/2$, $I = 1/2$ spin systems. *J. Magn. Reson. 144*, 228−242.
(39) Hagen, W. R. (1989) g-strain: Inhomogeneous broadening in metalloprotein EPR, in *Advanced EPR: Applications in Biology and Biochemistry* (Hoff, A. J., Ed.), pp 782−812, Elsevier, Amsterdam.
(40) Froncisz, W., and Hyde, J. S. (1980) Broadening by strains of lines in the g-parallel region of Cu^{2+} EPR spectra. *J. Chem. Phys. 73*, 3123−3131.

DOI: 10.1021/acs.biochem.5b00528
Biochemistry 2015, 54, 5030−5044

(41) Dunham, W. R., and Sands, R. H. (2003) g-Strain, ENDOR, and structure of active centers of two-iron ferredoxins. *Biochem. Biophys. Res. Commun. 312*, 255−261.
(42) Reijerse, E. J., and Dikanov, S. A. (1991) Electron spin echo envelope modulation spectroscopy on orientationally-disordered systems: Line shape singularities in $S = 1/2$, $I = 1/2$ spin systems. *J. Chem. Phys. 95*, 836−845.
(43) Lin, M. T., Sperling, L. J., Frericks Schmidt, H. L., Tang, M., Samoilova, R. I., Kumasaka, T., Iwasaki, T., Dikanov, S. A., Rienstra, Ch. M., and Gennis, R. B. (2011) A rapid and robust method for selective isotope labeling of proteins. *Methods 55*, 370−378.
(44) Gardiner, A. T., Zech, S. G., MacMillan, F., Käss, H., Bittl, R., Schlodder, E., Lendzian, F., and Lubitz, W. (1999) Electron Paramagnetic Resonance studies of zinc-substituted reaction centers from *Rhodopseudomonas viridis*. *Biochemistry 38*, 11773−11787.
(45) Taguchi, A. T., O'Malley, P. J., Wraight, C. A., and Dikanov, S. A. (2014) Nuclear hyperfine and quadrupole tensor characterization of the nitrogen hydrogen bond donors to the semiquinone of the Q_B site in bacterial reaction centers: A combined X- and S-band ^{14,15}N ESEEM and DFT study. *J. Phys. Chem. B 118*, 1501−1509.
(46) Grimaldi, S., Arias-Cartin, R., Lanciano, P., Lyubenova, S., Endeward, B., Prisner, T. F., Magalon, A., and Guigliarelli, B. (2010) Direct evidence for nitrogen ligation to the high stability semiquinone intermediate in *Escherichia coli* nitrate reductase A. *J. Biol. Chem. 285*, 179−187.
(47) Deligiannakis, Y., Hanley, J., and Rutherford, A. W. (1999) 1D- and 2D ESEEM study of the semiquinone radical Q_A^- of Photosystem II. *J. Am. Chem. Soc. 121*, 7653−7664.
(48) Astashkin, A. V., Hara, H., Kuroiwa, S., Kawamori, A., and Akabori, K. (1998) A comparative electron spin echo envelope modulation study of the primary electron acceptor quinone in Zn-substituted and cyanide-treated preparations of Photosystem II. *J. Chem. Phys. 108*, 10143−10151.
(49) Dikanov, S. A., Holland, J. T., Endeward, B., Kolling, D. R., Samoilova, R. I., Prisner, T. F., and Crofts, A. R. (2007) Hydrogen bonds between nitrogen donors and the semiquinone in the Q_i-site of the bc_1 complex. *J. Biol. Chem. 282*, 25831−25841.
(50) O'Malley, P. J., and Babcock, G. T. (1986) Powder ENDOR spectra of p-benzoquinone anion radical: Principal hyperfine tensor components for ring protons and for hydrogen-bonded protons. *J. Am. Chem. Soc. 108*, 3995−4001.
(51) MacMillan, F., Lendzian, F., and Lubitz, W. (1995) EPR and ENDOR characterization of semiquinone anion radicals related to photosynthesis. *Magn. Reson. Chem. 33*, S81−S93.
(52) Flores, M., Isaacson, R. A., Calvo, R., Feher, G., and Lubitz, W. (2003) Probing hydrogen bonding to quinone-anion radicals by ^{1}H and ^{2}H ENDOR spectroscopy. *Chem. Phys. 294*, 401−413.
(53) Sinnecker, S., Reijerse, E., Neese, F., and Lubitz, W. (2004) Hydrogen bond geometries from Electron Paramagnetic Resonance and Electron-Nuclear Double Resonance parameters: Density Functional study of quinone radical anion-solvent interactions. *J. Am. Chem. Soc. 126*, 3280−3290.
(54) Lin, T.-J., and O'Malley, P. J. (2008) An ONIOM study of the Q_A site semiquinone in the *Rhodobacter sphaeroides* photosynthetic reaction centre. *J. Mol. Struct.: THEOCHEM 870*, 31−35.
(55) Rohrer, M., MacMillan, F., Prisner, T. F., Gardner, A. T., Möbius, K., and Lubitz, W. (1998) Pulsed ENDOR at 95 GHz on the primary acceptor ubisemiquinone Q_A^- in photosynthetic bacterial reaction centers and related model systems. *J. Phys. Chem. B 102*, 4648−4657.
(56) Martin, E., Baldansuren, A., Lin, T.-J., Samoilova, R. I., Wraight, C. A., Dikanov, S. A., and O'Malley, P. J. (2012) Hydrogen bonding between the Q_B site ubisemiquinone and Ser-L223 in the bacterial reaction center − a combined spectroscopic and computational perspective. *Biochemistry 51*, 9086−9093.
(57) Schnegg, A., Dubinskii, A. A., Fuchs, M. R., Grishin, Yu. A., Kirilina, E. P., Lubitz, W., Plato, M., Savitsky, A., and Möbius, K. (2007) High-Field EPR, ENDOR and ELDOR on bacterial photosynthetic reaction centers. *Appl. Magn. Reson. 31*, 59−98.
(58) Lin, T.-J., and O'Malley, P. J. (2011) Binding site influence on the electronic structure and Electron Paramagnetic Resonance properties of the phyllosemiquinone free radical of Photosystem I. *J. Phys. Chem. B 115*, 9311−9319.
(59) Niklas, J., Epel, B., Antonkine, M. L., Sinnecker, S., Pandelia, M.-E., and Lubitz, W. (2009) Electronic structure of the quinone radical anion $A1^{\bullet-}$ of Photosystem I investigated by advanced Pulse EPR and ENDOR techniques. *J. Phys. Chem. B 113*, 10367−10379.
(60) Srinivasan, N., Chatterjee, R., Milikisiyants, S., Golbeck, J. H., and Lakshmi, K. V. (2011) Effect of hydrogen bond strength on the redox properties of phylloquinones: A two-dimensional Hyperfine Sublevel Correlation Spectroscopy study of Photosystem I. *Biochemistry 50*, 3495−3501.
(61) Gardiner, A. T., Zech, S. G., MacMillan, F., Käss, H., Bittl, R., Schlodder, E., Lendzian, F., and Lubitz, W. (1999) Electron Paramagnetic Resonance Studies of Zinc-Substituted Reaction Centers from *Rhodopseudomonas viridis*. *Biochemistry 38*, 11773−11787.
(62) Grimaldi, S., Arias-Cartin, R., Lanciano, P., Lyubenova, S., Szenes, R., Endeward, B., Prisner, T. F., Guigliarelli, B., and Magalon, A. (2012) Determination of the proton environment of high stability menasemiquinone intermediate in *Escherichia coli* nitrate reductase A by pulsed EPR. *J. Biol. Chem. 287*, 4662−4670.
(63) Morton, J. R., and Preston, K. F. (1978) Atomic parameters for paramagnetic resonance data. *J. Magn. Reson. 30*, 577−582.
(64) Bratt, P. J., Ringus, E., Hassan, A., van Tol, H., Maniero, A.-L., Brunel, L.-C., Rohrer, M., Bubenzer-Hange, C., Scheer, H., and Angerhofer, A. (1999) EPR on biological samples beyond the limits of superconducting magnets—The primary donor cation of purple bacterial photosynthesis. *J. Phys. Chem. B 103*, 10973−10977.

DOI: 10.1021/acs.biochem.5b00528
Biochemistry 2015, 54, 5030−5044